DEM study of mechanical characteristics of multi-spherical and superquadric particles at micro and macro scales

DEM study of mechanical characteristics of multi-spherical and superquadric particles at micro and macro scales

Behzad Soltanbeigi[a], Alexander Podlozhnyuk[b,*], Stefanos-Aldo Papanicolopulos[a], Christoph Kloss[b,d], Stefan Pirker[c], Jin Y. Ooi[a]

[a]*Institute for Infrastructure and Environment, School of Engineering, University of Edinburgh, EH9 3JL, Edinburgh, UK*
[b]*DCS Computing GmbH, Industriezeile 35, 4020, Linz, Austria*
[c]*Department of Particulate Flow Modeling, Johannes Kepler University, Altenberger Strasse 69, 4040, Linz, Austria*
[d]*CFDEMresearch GmbH, Industriezeile 35, 4020, Linz, Austria*

Abstract

Multi-spheres and Superquadrics are popular approaches for addressing particle shape effect in the Discrete Element Method (DEM). This study focuses on the mechanical characteristics of cubical particles, modelled by the two methods (using EDEM and LIGGGHTS), through conducting a series of numerical case studies at both single particle and bulk levels. In the first part of the study, several testing scenarios, which clarify the impact, interlocking, sliding and tilting characteristics of the particle, are discussed and the respective simulations are carried out. The results emphasize the importance of surface bumpiness and edge sharpness in the single-particle behaviour and are used for informing the bulk response.

Further, role of the two shape descriptors on bulk response is evaluated in angle of repose, Jenike shear and silo flow simulations. The results of these tests are assessed both at the micro, directly through DEM outputs, and at the meso- and macro- scales, using a coarse graining technique. It is seen that the properties of edge and surface in superquadric and multi-sphere particles considerably influence the heap profile in the angle of repose test. However, in a Jenike direct shear, the shape complexity only significantly affects the shear strength, porosity and mode of motion when the packing is dense. Additionally, in silo discharge, the effect of shape features is even less on the flow pattern and mass flow rate but is found to have a significant influence on the stress distribution.

Keywords: Superquadric, Multi-sphere, Multi-scale, Coarse-graining, Jenike shear tester, Silo

1. Introduction

The growth in computational power has increased the popularity of the Discrete Element Method (DEM) [1]. This powerful numerical tool is now more accessible to both industry and academia for modelling complicated particulate systems. In DEM, the granular material is treated as a system of distinct interacting particles. Accordingly, the velocity, position and contact properties of each particle are tracked individually.

An efficient particle shape representation is a key challenge in DEM. Most DEM codes use spherical particles to

*Corresponding author
Email address: alexander.podlozhnyuk@dcs-computing.com, Tel.: +43-732-9022-2200 (Alexander Podlozhnyuk)

reduce the computational cost of the simulations, although in reality particles are mostly of irregular shape. Several non-spherical shape descriptors have been proposed in the literature, the most popular approach in DEM being the multi-sphere approach (MS) [2, 3, 4, 5, 6, 7, 8]. In this description, spheres are allowed to overlap and be glued together to approximate an arbitrarily shaped particle. On the other hand, irregular particle shapes can alternatively be idealized to some regular shapes such as spheroids, cuboids or cylinders that can be approximated by superquadric (SQ) shapes [9, 10, 11]. It has been suggested that 80% of all shapes can be represented by superquadric functions or derived from superquadrics in higher-dimensional hyperquadrics [12, 13]. SQ particles demonstrate an excellent trade-off between model complexity and shape flexibility. Changing only five shape parameters gives an opportunity to switch from a spherical particle to an ellipsoidal, cylindrical or box-like particles. These particle shapes are able to capture many physical elements of real particles and extend the range of applicability of DEM.

Following is a summary of the studies that have focused on the characteristics of different shape representation methods and compared them at the micro and macro levels:

Matsushima and Saomoto [14] pointed out the lack of a method which enables the implementation of real shape for sand grains in DEM simulations. They proposed an algorithm to obtain optimum sizes and positions of sub-elements (circles in 2-D and spheres in 3-D) for describing an irregular particle shape. Accuracy and convergence of this algorithm is further discussed through conducting a bi-axial element test.

Mollanouri Shamsi and Mirghasemi [15] utilized MS particles to investigate the influence of particle angularity on the bulk response of a granular assembly in a triaxial test. They observed that the more angular the single particles are (at a specified confining pressure), the higher mobilized friction angle and dilation is reached. Additionally, they reported that the shear strength is more affected by angularity once higher friction coefficients are applied.

Ouadfel [16] has implemented and validated an algorithm for inter-ellipsoid contact detection. He conducted a number of constant mean pressure deviatoric compression tests on assemblies of ellipsoidal particles to study the importance of size, shape, inherent anisotropy and confining pressure on the macro-scale response of ellipsoids.

Kruggel-Emden et al.[17] modeled a spherical particle hitting a flat wall. The sphere was modeled as a single rigid sphere and as a multi-sphere particle composed by smaller sub-spheres. It was shown that macroscopic collision properties derived from MS simulations strongly depend on the alignment of the particle. The authors show that the MS method has certain limitations when used for the approximation of a spherical body and therefore could face difficulties when applied to other arbitrary shapes.

Höhner et al.[18] studied the adequacy of the MS and polyhedral (PH) approach to approximate particle-wall collisions of ellipsoidal particles. They showed that both approaches require significantly less computational time compared to the ellipsoid contact algorithm while still yielding acceptable results at micro-level.

Höhner et al.[19, 20] conducted DEM simulations with spherical, PH and MS particles and examined the macroscopic features of the flow during hopper discharge. The results revealed that polyhedral particles increase the flow resistance compared to MS particles, and suggested that this might be due to the relatively smooth surfaces of the MS

particles, while PH surfaces have multiple sharp vertices and edges. Moreover, Höhner et al.[19] stated that smoother particles form a V-shaped flow that reaches the hopper walls, while increasing the angularity of the particles leads to a core flow above the opening. They also mentioned that particles with sharper edges have a tendency to build arches that can clog the flow.

Cleary and Sawley [21] compared the discharge of SQ and spherical particles from a hopper and showed that the non-sphericity causes a slower flow up to 30% and also changes the flow kinematics. They found that the hopper flows are not sensitive to any further increase of particle angularity if SQ blockiness N is greater than 8.

Pereira and Cleary [22] studied segregation of binary granular mixture composed by cubes modeled as SQ and spheres in a slowly rotating cylindrical tumbler. They found that cubical particles segregate to the inner core of the particle bed while the spherical particles segregate to the curved walls of the tumbler. It was shown that blocky particles dissipate energy faster than spherical ones and hence move more slowly as they travel down the free surface.

Fraige et al. [23] simulated spherical and cubical particles in a flat-bottom silo and concluded that cubic-shape particles provide a packing with higher porosity and increased resistance to flow compared to spheres.

Härtl and Ooi [24], considering spherical and non-spherical (consist of two glued beads), investigated the influence of particle shape and on the bulk friction in a Jenike direct shear test. It is shown that particle interlocking has a more pronounced impact than porosity on the bulk friction.

Tao et al. [25] used the MS approach to represent corn-shape particles and compared the flow properties with spherical particles. They showed that the downward velocity of the clusters shows higher variation, compared to spheres, along the width of the silo (the maximum is seen in the centre and decreases towards the walls). Furthermore, they observed that the mean voidage of packings for non-spherical particles is smaller than that of the spherical particles.

Markauskas et al.[6] evaluated the capability of MS method to describe ellipsoidal particles, which can replace the perfectly smooth ellipsoids generated using the SQ technique. Varying the number of sub-spheres, the MS particles were characterized through studying the angle of repose, porosity and coordination numbers. They observed a non-linear increase of computational time with the increase in the number of sub-spheres compared to the case of ideal spherical particles. It was pointed out that increasing the number of sub-spheres exhibits a clear tendency to mimic macroscopic parameters of a smooth ellipsoid.

The studies summarised above show that several attempts have been made to understand the characteristics of different shape approximation methods. However, there is still a lack of a comprehensive study that investigates the bulk response of the SQ and MS particles under various compression and shearing conditions. Accordingly, this paper aims to provide a better understanding of the micro/macro properties of the MS and SQ particles and also investigates the potential similarities. In this respect, a series of grain level tests and as well as shearing tests in a Jenike shear tester with MS and SQ particles are conducted to determine the role of blockiness in SQ and number of sub-spheres (surface bumpiness) in MS particles. Subsequently, the influences of particle edge sharpness and surface roughness on

flow characteristics of a granular assembly are investigated. Eventually, attempts have been made for estimation of the flow characteristics based on the shear test results (i.e. numerical calibration).

2. Methodology

This section provides information regarding the material properties and the testing procedures that have been followed. The considered particles have cubical shapes with an edge length of $d = 2$mm (the reason for choosing cubical geometry is to have the aspect ratio as 1 and put emphasis on the surface and edge properties). Cubes were approximated by SQ particles in LIGGGHTS and by MS particles in EDEM [26] (except for Section 4.1, where MS particles were simulated in LIGGGHTS software). Regarding the use of two distinct DEM codes, it should be noted that the contact detection algorithm and force calculation methodology are different for multi-sphere and superquadric particles. Furthermore, using spherical particles, the consistency of the test conditions for both DEM codes was assessed through comparing the results of several single-particle and bulk-level tests (as also mentioned in the Section 4.2).

To simulate a perfect cube, the shape description method must be able to provide sharp edges. Theoretically, the edge sharpness of MS particles could be increased by using spheres of smaller size to represent the particle edges. However, this would lead to i) smaller time-step ii) higher number of sub-spheres per particle and, as a result, iii) higher computational costs. The current study evaluates whether surface bumpiness can compensate the lack of edge sharpness for MS particles approximating cubical particle.

The parameters for considered material are chosen in a way that the computational cost is reasonable. Table 1 shows the material properties for particles and the geometry. Hertz model with viscous damping (modified by Brilliantov et al.[27]) and Mindlin-Deresiewicz[28] model are used in all simulations as normal and tangential force models:

$$\begin{aligned} F^n &= k^n \delta^n - \gamma^n U^n \\ F^t &= \min(k^t \delta^t - \gamma^t U^t, \mu_s F^n) \end{aligned} \tag{1}$$

where δ_n is the normal overlap distance between particles, U^n is the normal component of the relative velocity at the contact point, δ^t is the tangential overlap[29], μ_s is the coefficient of sliding friction. Corresponding expressions for coefficients $k_n, k_t, \gamma_n, \gamma_t$ can be found in [30, 31, 10].

2.1. Superquadrics

The equation that governs the shape of a SQ particle in its local coordinate system, given by Barr [32], is as follows:

$$f(x,y,z) \equiv \left(\left| \frac{x}{a} \right|^{n_2} + \left| \frac{y}{b} \right|^{n_2} \right)^{\frac{n_1}{n_2}} + \left| \frac{z}{c} \right|^{n_1} - 1 = 0, \tag{2}$$

where a, b, c are the half-lengths of the particles along its principal axes, and n_1 and n_2 are blockiness parameters that control edge sharpness. Cubical particles can be modeled by superquadrics taking $a = b = c = d/2$ and taking

$n_1 = n_2 = N > 2$, where N controls the level of edge sharpness/blockiness. It is worth noting that each k-th SQ particle in a simulation can have its own set of parameters $(a_k, b_k, c_k, n_{1k}, n_{2k})$ and, as a result, corresponding shape function $f_k(x, y, z)$.

The contact detection algorithm is based on finding a "midway" point $\boldsymbol{X}_0$ between two superquadric particles A and B (Fig.1) that is a solution of the following non-linear system:

$$\begin{cases} \nabla F_A(\boldsymbol{X}) + \mu^2 \nabla F_B(\boldsymbol{X}) = 0 \\ F_A(\boldsymbol{X}) - F_B(\boldsymbol{X}) = 0, \end{cases} \tag{3}$$

where μ is the proportionality coefficient, $F_k(\boldsymbol{X}) = f_k(\boldsymbol{Q}_k^T \cdot (\boldsymbol{X} - \boldsymbol{X}_{Ck}))$ is the shape function of particle k defined with respect to a global coordinate system, $\boldsymbol{X}_{Ck}$ is the centre of mass, $\boldsymbol{Q}_k = \boldsymbol{Q}(\boldsymbol{q}_k)$ is the quaternion-based rotation matrix and $\boldsymbol{q}_k$ is the quaternion that tracks orientation of particle k. The contact direction $\boldsymbol{n}_{AB} = \nabla F_A / ||\nabla F_A||$ is calculated at the contact point $\boldsymbol{X}_0$. The normal overlap vector $\boldsymbol{\delta}_n$ is defined as a vector connecting points of intersection $\boldsymbol{X}_B$ and $\boldsymbol{X}_A$ between the contact line and surfaces of particles A and B correspondingly:

$$\begin{aligned} &F_A(\boldsymbol{X}_A) = 0, \text{where } \boldsymbol{X}_A = \boldsymbol{X}_0 + \alpha_A \boldsymbol{n}_{AB}, \\ &F_B(\boldsymbol{X}_B) = 0, \text{where } \boldsymbol{X}_B = \boldsymbol{X}_0 + \alpha_B \boldsymbol{n}_{AB}, \\ &\boldsymbol{\delta}_n \equiv \boldsymbol{X}_A - \boldsymbol{X}_B = (\alpha_A - \alpha_B)\boldsymbol{n}_{AB}. \end{aligned} \tag{4}$$

Standard normal and tangential force models[30] can be applied, using local curvature radius as particle radius in force formulations.

Newton's method is employed to solve the system of non-linear equations (3) for every potential pair of particles at every DEM time-step. Several techniques can be proposed to reduce the number of potential particle pairs and increase computational efficiency: checking intersections between minimum bounding spheres and oriented bounding boxes, and using the solution for the contact point from the previous step at a current step as initial guess. Eq. (4) must be solved for every pair of overlapping particles. For a more detailed description of contact detection and a contact force algorithms between SQ particles refer to Podlozhnyuk et al. [10].

Different levels of edge sharpness (between $N = 4$ and $N = 10$, further denoted as SQ($N4$),...,SQ($N10$)) are used in this paper to study the blockiness effect. Fig.2 (top row) illustrates particle shapes for SQ($N4$), SQ($N6$) and SQ($N8$).

2.2. Multi-sphere approach

Multi-spheres, which approximate the shape of particles by overlapping or touching spheres, are used as an approximation of the real shape irregularities [3, 33]. In the multi-sphere model, a single particle is represented by a set of rigidly connected spheres, which are inscribed into the shape of the particle such that at each contact point of sphere and real body a tangential plane can be constructed. The sub-spheres are allowed to vary in size and to overlap forming an approximation of any desired shape. The contact force between neighboring particles is calculated from

their element spheres, using sphere-sphere contact detection. Each sub-sphere i of particle A is checked for contact against each sub-sphere k of particle B(see Fig.3). The normal overlap vector δ_{ABik} is determined for each pair of intersecting sub-spheres in the same way as conducted for single spherical particles:

$$\begin{aligned} \delta_{ABik} &= \|\boldsymbol{X}_{Ai} - \boldsymbol{X}_{Bk}\| - (r_{Ai} + r_{Bk}) \\ \boldsymbol{X}_{Ai} &= \boldsymbol{X}_{CA} + \boldsymbol{Q}_A \cdot \boldsymbol{d}_{Ai} \\ \boldsymbol{X}_{Bk} &= \boldsymbol{X}_{CB} + \boldsymbol{Q}_B \cdot \boldsymbol{d}_{Bk}, \end{aligned} \tag{5}$$

where $\boldsymbol{X}_{CA}$ and $\boldsymbol{X}_{CB}$ are the centres of gravity, $\boldsymbol{Q}_A$ and $\boldsymbol{Q}_B$ are the rotational matrices converting vectors from the body-fixed frame to the global coordinate system, $\boldsymbol{d}_{Ai}$ and $\boldsymbol{d}_{Bk}$ are the vectors in the body-fixed frame pointing from the centres of gravity ($\boldsymbol{X}_{CA}$ and $\boldsymbol{X}_{CB}$) to the centres of sub-spheres i and k for multi-sphere particles A and B correspondingly.

Contact forces F_{ABik} are obtained from the calculated overlaps δ_{ABik} for each pair of overlapping sub-spheres between particles A and B. The resulting overall force acting on particle A from particle B is determined as follows:

$$\boldsymbol{F}_{AB} = \sum_{i,k:\delta_{ABik}<0} \boldsymbol{F}_{ABik}. \tag{6}$$

Details of the algorithm and mechanical calculations can be found in Abbaspour-Fard and Favier et al. [2, 3].

Cubes, as multi-spheres, were modeled in EDEM software using equal-radius ($d/4$) overlapping sub-spheres. The number of sub-spheres in each edge of the cubes varies between 2 and 5, resulting in 8, 27, 64, and 125 total sub-spheres per particle (further denoted as MS(8), MS(27), MS(64) and MS(125) correspondingly). Graphical illustrations for MS(8), MS(27), MS(64) are given in Fig. 2 (bottom row).

2.3. Coarse-graining

In order to compute the continuum fields through micro-scale data, an appropriate averaging methodology must be followed. The average procedure captures the fluctuation of the continuum fields and allows the continuum parameters of interest to be evaluated at appropriate local spatio-temporal scales. In this study, we are using the averaging or coarse graining (CG) technique described by [34] to obtain macro-scale features of the granular assembly such as density, velocity and stress.

Coarse-graining utilizes both spatial and temporal options for averaging the DEM results, in which the former regulates the extent of the volume contributing to the field data at each point and the latter is employed to represent the temporal fluctuations [34].

Both the spatial (w) and the temporal (ΔT) scales are problem-dependent and vary with the dynamic characteristics of the granular system. However, based on studies conducted by the authors and also as suggested by Weinhart

et. al[35], values of $d < w < 2d$ are appropriate for quasi-statics systems. Additionally, to reduce the instantaneous fluctuations, a temporal average over $\Delta T = 0.5s$ with a 100Hz data output frequency has been applied to the spatially averaged results.

3. Simulation results: micro-level

3.1. Particle-wall impact

In this test, a particle impacts a flat wall with a specified translational velocity ($v_{pre} = 0.01$m/s) normal to the wall and zero angular velocity. The particle has one plane of symmetry parallel to the wall, so that face-wall contact occurs. The post-impact particle velocity v_{post} normal to the wall is computed. The contact is assumed to be frictionless and without gravity. It can be observed from Fig. 4 that for all particle shapes used the velocity increases again until a certain point, as expected, but then it decreases again slightly. This occurs due to the employed viscous damping model at the end of the contact, when the repulsive force in Eq.(1) ($k\delta^n$) component becomes smaller than the viscous part ($\gamma^n U^n$) and the total normal force becomes aligned towards the wall, decreasing the rebound velocity. After the impact is finished, it is clear from Fig. 4 that the post-impact velocity for superquadric cubes does not depend on the blockiness parameter N and satisfies the coefficient of restitution: $v_{post}/v_{pre} = \varepsilon_{pw}$. On the contrary, the post-impact velocity for multi-spheres decreases with increasing number of sub-spheres. This is a well-known drawback of the standard multi-sphere method [17],[36], [18]. To overcome this problem the calculation of the contact forces has to be modified. The total force of the contacting sub-spheres cannot be equivalent to the contact force between contacting MS-particles. Kodam et al.[36] proposed to adjust the normal spring stiffness that minimizes the error between the summarized contact force of the sub-spheres and reference particle is minimized. An alternative solution as demonstrated by Kruggel-Emden et al. [17] would be to divide the total sum of all component forces by the number of contact points for each contact pair of MS-particles (advanced MS-method).

3.2. Degree of interlocking

Particle shape irregularity is quantified in the following section. Particle 1 and Particle 2 stand on a flat surface having centres at $(-r, 0, r)$ and $(r, 0, r)$ correspondingly and touching each other at $(0, 0, r)$, where $r = d/2$ is the half-edge length of a particle. Particle 3 is initially located at $(-r, 0, 3r)$ producing zero overlap, and is allowed to fall under gravity over Particle 1 (configuration "1+2", Fig.5).

The interlocking value $\delta z = 3r - z$ is calculated, where z is the residual Z-coordinate of the centre of Particle 3. Then, after impact, the initial position of Particle 3 in X-direction is changed by small $\delta x : x := x + \delta x$ and the simulations are iterated from $x = -r$ till $x = r$. The interlocking value δz as a function of initial position in X-direction is presented in Fig.6.

It is clear from Fig.6 that the MS(8) shape has the highest degree of interlocking as can be expected from the surface being represented by two spheres in contact. Moreover, δz decreases with the increase of the number of sub-

spheres. The degree of interlocking for SQ particles has its maximum for SQ($N4$) and decreases with the increase of superquadric blockiness N.

The effect of particle shape irregularity is further studied in the following set of simulations with 3 particles (in "1+2" configuration). Particle 1,2 and 3 are located initially exactly in the same way as in Fig.5. Particle 1 and 2 remain static during the whole simulation. Particle 3 moves from $x = -r$ to $x = r$ with prescribed constant translational velocity $u_x = 1$mm/s in X-direction, having 1 degree of freedom (along Z-axis, no rotation).

3.3. Particle-Particle sliding

The simulation is conducted for different friction coefficients: $\mu^s_{pp} = 0.1, 0.3, 0.56$. Tangential force F_t acting on Particle 3 is calculated as the x-component of the total force (normal+tangential) taken with the negative sign ($-F_x$). In order to cancel out the effect of different masses per single particle, it is plotted (Fig.7) in dimensionless form ($F_t/\mu^s_{pp}mg$) as a function of relative displacement x/r. The total mechanical work done by the tangential force F_t is added to the legend in dimensionless form:

$$W = A/A_0, A = \int_{-r}^{r} F_t dx, \tag{7}$$

where $A_0 = 2\mu^s_{pp}mgr$ is the mechanical work done by the friction force for a displacement $\Delta x = 2r$ (from $x = -r$ to $x = r$), assuming particles as ideal cubes sliding along a flat surface. It can be seen from Fig.7 that the behaviour of the tangential force for MS particles exhibits "zigzag" pattern. For SQ particles there is always only one local maximum/minimum that is related to the gap at $x = 0$ between particles 1 and 2. It seems that the behaviour of MS and SQ particles (maximum tangential force F_t and its mechanical work) tends to converge to that for ideal cubes ($F_t = \mu^s_{pp}mg = const, A = A_0$) with the increase of the number of subspheres (for MS) and blockiness N (for SQ) and with the increase of the friction coefficient μ^s_{pp}. However, significantly higher MS-particle resolution is required to achieve less than 5% of the maximum relative deviation of the tangential force from the mean value.

3.4. Inclined/rotating plate I

Here, a single particle is placed onto a flat surface that starts to rotate with constant angular velocity $\omega = \pi/50$ [rad/s]. The distance between rotation origin and projection of the particle centre onto the surface is $L = 24$mm (Fig. 8). For each particle shape the corresponding critical angle (the angle at which a particle begins to move/tilt) is found for coefficients of friction $\mu_1 = 0.45$ and $\mu_2 = 0.56$ and compared to the sliding angles $\alpha_1 = \arctan(\mu_1) = 24.23^\circ$ and $\alpha_2 = \arctan(\mu_2) = 29.25^\circ$.

Two scenarios are possible during the rotation of the plate: sliding of a particle along the plate without changing the orientation, or tilting of the particle towards the rotation origin. For the SQ particles (Fig.9), the results are depending on particle blockiness/edge sharpness (N). The SQ($N4$) and SQ($N5$) particles tilt and fall at the same angles irrespective of the coefficient of friction. For coefficient of friction $\mu = \mu_1$, SQ($N6$), SQ($N7$) and SQ($N8$)

particles slide at the sliding angle, while for $\mu = \mu_2$, the critical angle increases with the increase of blockiness N. The results show that particles with different levels of edge sharpness can behave differently even at the single grain level (changing the mode of motion from rotational to translational).

It is interesting to note that the behaviour of MS particles does not depend on the number of sub-spheres. For μ_1, MS particles begin to slide exactly at the sliding angle α_1; for μ_2, they begin to tilt and fall from the plate at around 27° (similar to SQ($N6$)), irrespective of the number of sub-spheres for both values of the coefficient of friction studied. This can be explained by the fact that all MS particles have sub-spheres with equal sizes, which give them an alike tilting characteristics.

3.5. Inclined/rotating plate II

In this simulation, 3 particles in configuration "1+2" stand on a flat surface. Particle 3 is standing exactly above the gap between particles 1 and 2 (Fig.10). The flat surface starts to rotate and the critical angle for particle 3 is measured. The angular velocity ω and the distance L between the rotation origin and the gap between particles 1 and 2 are exactly the same as in the previous section. The particle-wall friction coefficient $\mu^s_{pw} = 1$ was chosen to avoid sliding of particles 1 and 2 along the flat surfaces before particle 3 starts moving. The coefficient of friction between particles was varied: $\mu^s_{pp} = 0.1, 0.2, 0.3, 0.4$, and 0.56. Critical angle as a function of superquadric blockiness (N) and the number of sub-spheres is presented in Fig.11. MS(216), MS(343) and MS(729) particles (with 6, 7 and 9 sub-spheres per edge correspondingly) have been additionally simulated. The simulation results ("S") are compared with the analytical solution ("A", case of perfect cubes): $\alpha_{crit} = \arctan(\mu^s_{pp})$ that covers only particle sliding.

It is clear, behaviour for SQ converges to that for ideal cubes with the increase of blockiness for all coefficients of particle-particle friction (μ^s_{pp}) used. Starting from $N = 8$ the results can be considered as converged to α_{crit}. At low blockiness ($N = 4$) there is a maximum 50% deviation from α_{crit}. For MS particles, there are significant errors at low μ^s_{pp} and low number of sub-spheres due to high particle interlocking level/bumpiness. Moreover, it seems that the results for most of the μ^s_{pp} tend to converge to values that differ from α_{crit} with increasing the number of sub-spheres. Similar to section 3.3, a significantly larger number of sub-spheres can be required to consider results as converged for coefficients of friction between 0.2 and 0.4. For $\mu^s_{pp} = 0.56$ the critical angle does not depend on the number of sub-spheres significantly converging to a value slightly lower than α_{crit}.

Based on the results above and the results from previous sections, we can conclude that at low coefficients of friction (≤ 0.2) representation of particle shape using SQ and MS can have significant effect on particle motion, especially for MS particles (interlocking effect). At high contact friction, the effect of particle-interlocking can be relatively neglected.

4. Simulation results: macro-level

4.1. Angle of repose

In this test an assembly of 6000 particles is distributed randomly in a cone. The system is allowed to settle under gravity (in Z-direction) for 1s simulation time. Fig.12 shows the simulation setup and the dimensions used.

The average residual translational and angular velocities for MS particles after settling were found to be of order $v_{ave}^{MS} = 10^{-13}$m/s and $\omega_{ave}^{MS} = 10^{-9}$rad/s correspondingly, while for SQ particles the velocities were around $v_{ave}^{SQ} = 10^{-5}$m/s and $\omega_{ave}^{MS} = 10^{-2}$rad/s. A possible explanation for this can be bumpiness of MS particles that produces an artificial sliding and rolling resistance because of multiple contact points between two MS particles. Concerning SQ particles, the contact is based only on a single contact point. Stability of the packings for SQ particles can be increased by applying a rolling friction model, like models B and C in [37], with a relative small rolling friction coefficient about $\mu_r = 10^{-3}$ or $\mu_r = 10^{-2}$ to dissipate energy. In this case the average residual translational and angular velocities for SQ particles were found to be around one order less for $\mu_r = 10^{-3}$ and 4 orders less for $\mu_r = 10^{-2}$ correspondingly with respect to zero rolling friction coefficient. However, the influence of a small rolling friction coefficient on the superquadric DEM simulation results must be further studied. Hence, zero rolling friction coefficient is used in all simulation results presented further in this paper.

Then, after the packing is formed, the orifice is opened and discharge commences. The simulation continues for 3s until a heap is formed. The heap is then analysed and the angle of repose is estimated.

The algorithm that determines the angle of repose of the heap operates by dividing the heap along Z-direction into 20 discs of equal height (instead of dividing into wedge shaped regions as in [38]). The discs are allowed to overlap by 50% with the neighbors in vertical direction. Then, the average cross-sectional area S_i of each disc is calculated by constructing a convex hull from particle centres in the XY plane. Each disc is assumed to be cylindrical with area equivalent radius $r_i = \sqrt{S_i/\pi}$. This way, it was possible to construct the surface profile function $z_i = z(r_i)$ and plot it for each of particle shapes, see Fig.13.

Furthermore, the angle of repose is found as the inclination angle of $z = z(r)$ using linear regression, see Fig.14. The first and the last bins are excluded to avoid the influence of the rounded top and flattened foot of the heap. It can be seen from Fig. 14 that the results for SQ particles are located within a larger interval than MS particles. The increase of SQ blockiness parameter N from $N = 4$ to $N = 8$ increases monotonically the angle of repose. Meanwhile, it is clear that, for MS particles, increasing the number of sub-spheres decreases bumpiness (which presumably would affect the angle of repose). Looking at Fig. 14, it is clear that there is an abrupt change for AOR of MS particles with 2 and 3 particles per edge (i.e. MS8 and MS27). However, it seems that further increase in the number of particles per edge (in this case from 3 to 5), is not affecting the avalanching characteristics of MS particles. A similar effect was observed by Markauskas et al. [6] for ellipsoidal particles.

Eventually, it is interesting to note that despite the very different interlocking mechanism and surface characteristics between SQ($N8$) and MS(8), both particles show similar heap profiles. Nevertheless, SQ($N4$) and MS(64), which have

alike geometric characteristics (both have relatively similar rounded edges, and MS(64) is less bumpy and tend to have a rather smooth surface), present very distinct heap profiles. It can be said that even small surface bumpiness can affect the heap formation of cubic particles (MS(64) has larger AOR than SQ($N4$) and SQ($N6$)). Additionally, it is seen that the SQ particles are more sensitive in AOR test on blockiness parameter.

In order to measure computational efficiency of MS and SQ approaches, the simulations for "Angle of Repose" with SQ and MS particles were conducted on the same machine using the same software (LIGGGHTS). Fig.15 illustrates performance degradation C_T/S_t as a function of the number of sub-spheres S_s for MS particles and as a function of blockiness N for SQ-particles, with C_T being the total computational time and S_T being the total simulation time with perfect spheres (can be considered as MS(1)). MS37 and MS61 particles, that are MS64 and MS125 particles with removed interior sub-spheres, were additionally simulated. It can be observed that the computational time for MS particles depends linearly on the number of sub-spheres with a factor of 1.3. MS(125) particles demonstrate the highest computational time and are excluded from further simulations. The total computational time for SQ particles is $10X$ larger than for the case of perfect spheres and it does not grow with the increase of blockiness N (being comparable to C_T of MS8 particles).

Based on the results above and the results from previous sections, only SQ($N4$), SQ($N6$), SQ($N8$) and MS(8), MS(27), MS(64) particles will be used further in this paper and compared to each other.

4.2. Jenike shear tester

The Jenike shear tester is widely used for measuring flow properties of particulate solids, [24]. In this test the granular material is placed in a split cylindrical box. Then, the material is consolidated by applying a constant vertical load σ_ν (10 kPa) to the lid section (consolidation state). Later, the top half of the cylinder (ring) is sheared at a constant translational velocity (2 mm/sec), see Fig.16. The measured quantity is the force required for this movement that can be converted to an average shear stress τ. Velocity of the lid in LIGGGHTS is controlled by a standard PID controller[39] that compares the current acting force f_{total} with the predefined target value f_{SP}. In EDEM position and velocity of the lid is controlled by multi-body dynamics.

Before comparing MS and SQ particles, simulations with mono-sized spherical particles were conducted to prove equivalence of the setups in the LIGGGHTS and EDEM codes. Results showed a reasonably good agreement with a maximum difference of 3 % (for stress-displacement curves). This discrepancy can be explained by the difference in initial particle configuration within the generated packings and also the difference in the constant vertical load controller.

The DEM time-step was chosen as $\Delta t = 2 \cdot 10^{-6}$ s (5 % of Rayleigh time) in all simulations. Two types of packing, using MS and SQ particles, were generated to assess the dependence of the results on the density of the initial packing. In the dense packing, the particle-particle friction coefficient μ^s_{pp} was set to zero at the filling stage and changed back to $\mu^s_{pp} = 0.56$ before applying σ_ν. On the contrary, the loose packing had $\mu^s_{pp} = 0.56$ during the whole simulation. For all simulations, material properties were kept identical and packings of equivalent bulk volume were generated using

SQ($N4$), SQ($N6$), SQ($N8$) and MS(8), MS(27), MS(64) particles. In the following two sections (4.2.1 & 4.2.2), the effects of particle edge and surface properties on the packing density and mode of motion are evaluated. Successively, the shearing response of the particles is assessed in section 4.2.3.

4.2.1. Porosity

The porosity ϕ of the samples was measured by exporting the position of the lid at start and end of shearing. This scalar quantity is an indication of how densely the particles are packed in the system (i.e. by dividing the total volume of the voids over the volume of the shear tester). As mentioned before, the packings are prepared in dense and loose states by switching the friction coefficient to 0 and 0.56 respectively. Fig.17 presents the initial porosity of the samples at $D = 0$ (end of consolidation) and also the relative change of porosity at end of shearing ($\Delta\phi$). The porosity at D = 0 is referred to as "initial porosity" (ϕ_{init}) and $\Delta\phi$ is calculated as:

$$\Delta\phi = \frac{\phi_{end} - \phi_{init}}{\phi_{init}} \cdot 100\% \tag{8}$$

where, ϕ_{end} is the final porosity of the sample at $D = 6$ mm.

According to Table 2, by increasing N, the number of particles in both density states decrease up to 15 %. Moreover, looking at Fig. 17, it is clear that the reduction in number of particles is not affecting the initial porosity (ϕ_{init}) of the system (i.e. the extension of edges for SQ($N6$) and SQ($N8$) provides similar total particle volume as the assembly of SQ($N4$) particles) despite the differences in volumes per single particle (Table 3). It is also seen that the value $N = 4$ leads to the highest ϕ_{init} for SQ particles (more noticeable for the dense case) and further increase of N from 6 to 8 has no effect on the porosity of the sample.

Moreover, results suggest that the bumpiness, in MS particles, can affect the initial porosity of the system and leads to increase of ϕ_{init} in both density states (here, it must be noted that the MS(8) has a void between composing particles which is subtracted from the total voids of the system).

Furthermore, it is seen that all of MS particles provide higher initial porosities than for SQ particles. This is mostly due to the additional void that is available between adjacent overlapping spheres on the surface of the MS particle.

Another important phenomenon that happens during shearing of the granular samples is the dilation of the assemblies. The ϕ_{init} for the samples are plotted in Fig.17 with respect to the change in porosity ($\Delta\phi$) at $D = 6$ mm. It is seen that even the samples with initially loose configurations tend to dilate, which might be due to the high level of irregularity that the considered particles have (for both MS and SQ particles $\Delta\phi$ <10 %). On the other hand, the magnitude of $\Delta\phi$ in dense samples is 3 to 4 times larger than for the loose samples (as expected, the dilatant behaviour is more pronounced for the dense packings). Additionally, the increase in blockiness of the SQ particles increases the $\Delta\phi$ magnitude. Unlike this, the effect of bumpiness on dilatancy is not following a specific trend for the considered MS particles. While the difference of $\Delta\phi$ for MS(27) and MS(64) is relatively small, MS(8) presents the lowest $\Delta\phi$. This is due to the higher initial porosity in sample with MS(8) particles. The observed results are well

capturing the concept of dilation and its dependency on density state in critical-state theory [40, 41].

It is also useful to monitor the vertical displacement of the lid, during the shearing of the assembly, to determine the mode of volume change (i.e. contractive or dilative), see Fig 18.For the loose packing, SQ($N4$) and MS(8) have the lowest amount of lid displacement (this is due to the higher initial porosity, see Figure 16). Furthermore, loose packings are showing a slightly contractive behaviour initially, approximately up to 1.5 mm of the shear displacement, before starting to dilate.

In dense packings, the contraction of the assemblies seems to be insignificant and dilation is the dominant mode of volume change. For the MS particles, the bumpiness effect can be seen in further dilation of MS(27) compared to MS(64), however, MS(8) has the least volume increase due to its initial higher porosity. On the other hand, increase in the corner sharpness of SQ particles is contributing to increased dilation of the assembly during shearing.

Coarse-graining shows the local distribution of the porosity in the Jenike shear tester. Fig.19a presents the results for MS(8), with ϕ_{init}=0.5, at $D = 6$ mm. It can be seen that the lowest porosity is formed from top right to bottom left corner. Moreover, the distribution of the magnitude of normal contact forces is presented in Fig.19b. Results suggest the zone with lower porosity concentration and strong contact forces overlaps.

4.2.2. Mode of motion for the particles

The previous section provides information on the effect of surface bumpiness and edge sharpness on the packing density and the dilation of the particles at the initial and final state of a direct shear test. In the current section, an attempt is made to evaluate the mode of motion for the particles during the shearing. Accordingly, the cumulative rotation $\boldsymbol{\theta}_i$ and its magnitude θ_i, for each particle i, is recorded for all the tests:

$$\boldsymbol{\theta}_i(t) = \frac{1}{2\pi}\int_0^t \boldsymbol{\omega}_i d\tau, \theta_i = ||\boldsymbol{\theta}_i||, i = \overline{1, N_p}, \tag{9}$$

where, $\boldsymbol{\omega}_i$ is the angular velocity of particle i and N_p is the number of particles in the system.

Fig.20 shows the distribution of the cumulative rotation magnitude at $D = 6$ mm for MS(8) particles (since a similar trend was seen for other particles, only the result for MS(8), with $\phi_{init} = 0.57$, is shown here). It is clear that the rotation of the particles is localized in a layer with a thickness of two to three particles (most rotation belongs to the particles located in the shear band), in the mid height of the shearing cell (this is commonly observed in both MS and SQ particles). The obtained results are in line with the numerical study in [42]. Fig.20 also shows the dilatant behaviour of the particles, that leads to elevation of the ring.

Fig.21 compares the magnitude of the cumulative rotation for the dense samples at the end of the shearing. Results imply that for both SQ and MS particles the magnitude of cumulative rotation is independent of the bumpiness and blockiness.

However, for the loose packings, as shown in Fig.22, SQ($N8$) and MS(8) present the lowest cumulative rotation (true for higher magnitudes of cumulative rotation >0.075). The percentage of MS particles with cumulative rotation

magnitude less than or equal to 0.025 is clearly higher than the corresponding percentage for SQ particles, independently of bumpiness/squareness. Nonetheless, for the rest of the cumulative rotation magnitudes, MS and SQ particles show similar values. Consequently, it can be deduced that the additional bumpiness/blockiness results in constraining the rotation of the particles (during shearing) only in loose packings.

4.2.3. Shear strength

The corresponding shear stress curves for SQ and MS particles as a function of shear displacement (D) are shown in Fig. 23. It can be seen that, in loose packing, SQ($N4$) has the lowest peak strength during shearing. However, it can be noticed that after increasing the blockiness to $N = 6$, the material shows a higher strength, but a further blockiness (i.e. $N = 8$) plays no significant role in the shearing response of the SQ particles. Additionally, one might argue that in shearing strength of the granular material, the fact of packing density matters to a large extent. Looking at Fig. 17, it can be seen that for the loose packings, cubes with different values of N and various surface bumpiness (except MS(8)) have a similar values of ϕ_{init}.

For the loose packings of the MS particles, the MS(27) and MS(64), which have relatively similar surface roughness, show a comparable peak strength, while a slightly lower residual strength can be seen for the MS(64) (this is due to further smoothness in the surface of the particle). The MS(8) is providing a peak and residual strength larger than for MS(27) and MS(64), which is an indication of increased interlocking among the MS(8) particles. Moreover, a similar residual strength is seen for the following pairs 'SQ($N4$) and MS(64)', and 'SQ($N6$), SQ($N8$) and MS(27)'. According to the shown results, it can be seen that increasing particle bumpiness can compensate to some extent the effect of edge sharpness when approximating particles by multi-spheres. Additionally, comparing the observations here with those of in section 4.1, it is deducible that in dense shearing regimes having a relatively resembling geometry for the particles can be adequate to capture comparable bulk response from different shape representation techniques.

For the dense packing, increasing blockiness for SQ particles results in higher shear strength of the material. A similar response is seen for the MS particles when the number of sub-spheres is reduced (the influence is roughly 30 % for both particle types). It should be noted that due to the limitation of the displacement in the Jenike tester, the residual strength of the dense samples has not been fully recorded for the particles with the highest amount of bumpiness and blockiness (i.e. MS (8) and SQ ($N6$) and ($N8$)). Accordingly, an alternative way is followed to compare the shear strength of the samples: we compared the peak friction angle (Φ_p), which is obtained through dividing the maximum value of τ by σ_n. The results for all the shapes are summarized in Fig. 24. Considering the dense packings, MS(8) is in good agreement with SQ($N6$) and SQ($N8$), whereas SQ($N4$) reaches a similar peak as for MS(27) and MS(64). Additionally, in the loose samples, both MS(64) and MS(27) have Φ_p values close to SQ($N6$) and SQ($N8$). Consequently, it can be said that influence of blockiness is increased in dense sample (the Φ_p value for MS(8) is reached by SQ($N6$) and SQ($N8$), however Φ_p for SQ($N6$) and SQ($N8$) only equals MS(27) and MS(64) in loose samples).

A close look into residual strength of the samples in both density states shows that SQ($N4$) and MS(64) present a similar response. On the other hand, it is an established fact that the quasi-static silo discharge can be considered as

a dense flow regime (similar to that of Jenike test). Considering this, it is of high interest to investigate the possibility of predicting flow characteristics of the two particles through the shear tests. This will be discussed in detail in section 4.3.

Fig.25 presents the local distribution of the horizontal stress for the MS and SQ particles (results are only shown for the dense samples, in which a greater shear strength is developed). The pattern for the horizontal stress is similar to the distribution of local porosity and contact network shown in Fig.19. Despite the similar residual strength for SQ($N4$) and MS(64), the stress distribution pattern seems to be slightly different for these particles. In general, the increase in shear strength of the material due to change in particle shape can be seen clearly.

The detailed study of the bulk response in the current section and also in section 4.2.1 reveals the idea that: Whilst the effect of bumpiness and blockiness may show up more strongly in single particle verification and free flow conditions (e.g. avalanching), in many dense flow situations such as here, the exact shape representation is not so important for all packings (to produce the right shearing response). In other words, once a certain degree of the surface and edge complexities is addressed, further adjustment may not be necessary for predicting the behaviour of dense flow regimes (i.e. once a cube is made out of 3 sub-spheres per edge, increasing the number of sub-spheres to 4 or 5 will not greatly influence the overall behaviour; similarly, for SQ blocks, once an edge sharpness of N=6 is considered, further increase of blockiness is not essential to predict the behaviour of a perfect cube). Additionally, it should be noted that packing density plays a major role in determining the importance of the shape factor (the denser the packing, the more influential is the shape factor on shear strength and porosity of the granular assembly).

4.3. Silo flow

This section addresses two objectives: a) evaluating the dependency of quasi-static flow on edge and surface properties of the MS and SQ particles b) assessing the validity of the numerical calibration methodology (through comparing the flow characteristics of particles with similar shearing response in the Jenike test). In this respect, the discharge process of the particles has been monitored inside a flat-bottom silo, which has dimensions $50d \times 5d \times 100d$ in x, y, z directions correspondingly. Periodic boundary conditions are applied in the y direction. The orifice dimension is $10d \times 5d$.

A total of about 21 000 particles were generated in each software to model the filling and discharge of the flat-bottom silo. Particles above the height of 0.2 m in the silo were removed from simulations before discharge in order to have equal bulk volumes, see Table 4 for the detailed number of particles. Please note that to address the difference in the volume of the single MS particles, the density of the MS (8) particles has been changed from 4100 to 6279 kg/m^3, to provide a match of the mass of MS(8) particle to the mass of MS(27) particle.

4.3.1. Discharge process

The discharge rate of the MS and SQ particles are shown in Fig. 26, shows the effect of blockiness and bumpiness on the discharging process. It is evident that for the SQ particles, the increasing blockiness retards the flow resulting

in a decreasing flow-rate For the MS particles, increasing the surface bumpiness also results in a decreasing flow-rate However the effect of bumpiness on flow-rate appears to be much smaller with MS (27) and MS (64) converging to a similar flow-rate. Moreover, the drop in discharge rate, by increasing pseudo-bumpiness, is smaller than the effect of increased blockiness for SQ particles (blockiness is not well captured by bumpiness). Moreover, MS(64) and SQ($N4$) (with similar residual shearing response) present an overlapping discharge rates (i.e. the slope of cumulative discharged mass in Fig. 26). The above results are in line with the Beverloo's equation [43], which predicts the mass flow rate (M) according to the following equation:

$$M = C\rho\sqrt{g}(D_0 - kd)^{5/2}, \tag{10}$$

where, C is constant that depends on the coefficient of friction, ρ_b is the bulk density after filling, g is the gravitational acceleration, D_0 is the opening width, d is the particle diameter, k is generally known to be a constant that depends on particle shape. In this case, kd increases by further bumpiness and blockiness (which results in reduction of the effective orifice dimension). Another important point is that compared to the significant dependency of the shearing resistance ($\approx 30\%$) on the shape characteristics, discharge rate is affected less ($\approx 10\%$).

Simulation snap-shots have been taken at different instances of the discharged mass (M_D) to provide an insight into flow profiles for both particle types. Fig. 27 shows the particles inside the silo at 10, 30 and 60 % of the discharge. It can be seen that the flow profiles are a function of the geometry of the particles. Increasing blockiness and bumpiness leads to development of the flow channels to higher elevation (M_D=10 %). Moreover, it is clear that the transition height, of which there is mass flow above this height, is increased (it is important to determine this point, since the maximum horizontal stress distribution is developed in this region). Additionally, it is observable that changing blockiness from 4 to 8 has a small effect on the formation of the dead/not-flowing zones, see M_D=60 %. Unlike for SQ particles, increasing bumpiness leads to formation of larger dead-zones in adjacent of the silo walls (see results at M_D=60%). Additionally, comparing flow pattern for particles with similar shear strength (i.e. SQ($N4$) and MS(64), which were predicted in the direct shear simulations earlier) depicts the similarity of flow kinematics for both particle types. Accordingly, results of this section suggests that for the silo flow situation, which involves large displacement regimes (where residual strength dominates), representation of particle shape using MS or SQ particles can produce matching predictions as long as the relevant residual strength characteristics is captured.

In addition to the above remarks, results indicates that whilst significant differences in single particle behaviour have been shown between the two shape descriptors, they do not lead to significant discrepancy in silo flow kinematics.

4.3.2. Stress distribution

The horizontal (σ_{xx}) and vertical (σ_{zz}) stress distributions inside the silo are obtained through coarse graining as shown in Fig. 28 (at MD=30 %). Furthermore, it is an established fact that the continuum fields can be averaged over directions in which the flow is homogeneous. In this respect, since applied periodic boundary in depth of silo

provides a homogeneous flow, the results are averaged over y direction.

A close look at σ_{zz} distributions for MS and SQ particles reveals that the vertical stress is independent of the particle shape characteristics. Additionally, the highest magnitude of the σ_{zz} is developed adjacent to the walls in the stagnant zones (two column of high stress at both sides of the flow channel). This is due to presence of the strong arches in the mass flow region that exerts the overburden pressure to the particles near the side-walls (it is clear that the flow channel cannot carry significant vertical loads).

Furthermore, the σ_{xx} distribution is showing a reduction with the increase in N parameter and decrease of number of sub-spheres. For MS(64) and SQ($N4$) particles, even though a similar flow pattern and discharge rate is captured, the distribution of σ_{xx} differs.

5. Conclusion

In this work, the behaviour of SQ particles (in LIGGGHTS) with different blockiness/edge sharpness levels, and MS particles (in EDEM) with different numbers of sub-spheres (surface bumpiness), have been evaluated in single-grain and macro level tests.

At grain-level, several test cases were simulated with MS and SQ particles, which led to a better understanding of impact, interlocking, sliding and tilting characteristics of the single particles. These tests show the dependence of particle behaviour at the micro-scale on the particle edge and surface properties. For example, it has been shown that, at low friction coefficients, interlocking of MS particles can have significant effect on particle motion.

In the angle of repose test, the surface inclination of the formed piles increases monotonically with the increase in blockiness. A similar influence is seen by increasing the bumpiness in MS particles. Measuring the simulation time for particles with different shape properties, it is shown that the SQ blockiness has no significant influence on the computational costs. On the contrary, the computational time for MS particles strongly depends on the number of sub-spheres. It is seen that only MS(8) (among all MS particles) have computational time comparable to that for SQ particles, which is approximately 10 times slower than spherical particles. The use of SQ particles can therefore be beneficial for modelling non-spherical particles in DEM (especially for blocky types of particles).

Further assessment of bulk behaviour of the MS and SQ particles is performed through conducting the Jenike shear test. Results suggest that the surface roughness, in MS particles, and edge sharpness, in SQ particles, can dictate the material response only in certain density states. Namely, for porosity, dilation and shear strength of the material a dense packing is more susceptible to the variation in blockiness and bumpiness of particle.

For the silo flow, it is shown that the discharge rate, flow profiles and stress are affected by the shape to varying degrees. With increasing blockiness and surface bumpiness, the flow is retarded to some extent, of the order of 10 % in this study. Moreover, the horizontal stress reduces whilst the vertical stress is much less sensitive to the shape characteristics.

The flow properties of the particles with similar residual shear strength have been assessed and an identical flow

pattern and discharge rate is recorded. Nevertheless, the inherent difference in total number of contacts in MS particles (which acts as additional frictional resistance) could potentially give a different stress field.

An outlook to future research is to consider validation of the DEM results by considering non-spherical particles and conduct angle of repose, Jenike shear and silo discharge experiments. This way, it will be possible to validate the observations from this numerical investigation with measured physical responses of particulate systems.

Acknowledgements

This work has been carried out as a part of the T-MAPPP project, an EU-funded FP7 Marie Curie Initial Training Network under grant agreement no. ITN 607453. The financial support provided by the European Commission is gratefully acknowledged. The assistance received from Dr. John P. Morrissey is also acknowledged.

References

[1] P. A. Cundall, O. D. L. Strack, A discrete numerical model for granular assemblies, Géotechnique 29 (1) (1979) 47–65. doi:10.1680/geot.1979.29.1.47.
URL http://www.icevirtuallibrary.com/doi/10.1680/geot.1979.29.1.47

[2] M. Abbaspour-Fard, Discrete element modelling of the dynamic behaviour of non-spherical particulate materials, Ph.D. thesis, The University of Newcastle upon Tyne (2000).
URL http://ethos.bl.uk/OrderDetails.do?uin=uk.bl.ethos.324869https://theses.ncl.ac.uk/dspace/bitstream/10443/970/1/Abbaspour-Fard00.pdf

[3] J. Favier, M. Abbaspour-Fard, M. Kremmer, A. Raji, Shape representation of axi-symmetrical, non-spherical particles in discrete element simulation using multi-element model particles, Engineering Computations 16 (4) (1999) 467–480. doi:10.1108/02644409910271894.
URL http://dx.doi.org/10.1108/02644409910271894

[4] L. Vu-Quoc, X. Zhang, O. R. Walton, A 3-D discrete-element method for dry granular flows of ellipsoidal particles, Computer Methods in Applied Mechanics and Engineering 187 (99) (2000) 483–528. doi:10.1016/S0045-7825(99)00337-0.

[5] M. Kremmer, J. F. Favier, A method for representing boundaries in discrete element modellingpart I: Geometry and contact detection, International Journal for Numerical Methods in Engineering 51 (12) (2001) 1407–1421. doi:10.1002/nme.184.
URL http://doi.wiley.com/10.1002/nme.184

[6] D. Markauskas, R. Kačianauskas, a. Džiugys, R. Navakas, Investigation of adequacy of multi-sphere approximation of elliptical particles for DEM simulations, Granular Matter 12 (1) (2009) 107–123. doi:10.1007/

s10035-009-0158-y.
URL http://link.springer.com/10.1007/s10035-009-0158-y

[7] H. Kruggel-Emden, S. Wirtz, V. Scherer, A study on tangential force laws applicable to the discrete element method (DEM) for materials with viscoelastic or plastic behavior, Chemical Engineering Science 63 (2008) 1523–1541. doi:10.1016/j.ces.2007.11.025.

[8] R. Cabiscol, J. H. Finke, A. Kwade, Calibration and interpretation of {DEM} parameters for simulations of cylindrical tablets with multi-sphere approach, Powder Technology (2017) –doi:https://doi.org/10.1016/j.powtec.2017.12.041.
URL https://www.sciencedirect.com/science/article/pii/S0032591017309981

[9] P. W. Cleary, Large scale industrial DEM modelling, Engineering Computations 21 (2/3/4) (2004) 169–204. doi:10.1108/02644400410519730.
URL http://www.emeraldinsight.com/doi/abs/10.1108/02644400410519730

[10] A. Podlozhnyuk, S. Pirker, C. Kloss, Efficient implementation of superquadric particles in Discrete Element Method within an open-source framework, Computational Particle Mechanicsdoi:10.1007/s40571-016-0131-6.
URL http://link.springer.com/10.1007/s40571-016-0131-6

[11] B. Soltanbeigi, A. Podlozhnyuk, J. Y. Ooi, C. Kloss, S.-A. Papanicolopulos, Comparison of multi-sphere and superquadric particle representation for modelling shearing and flow characteristics of granular assemblies, in: European Physical Journal Web of Conferences, Vol. 140, 2017.

[12] W. Zhong, A. Yu, X. Liu, Z. Tong, H. Zhang, DEM/CFD-DEM Modelling of Non-spherical Particulate Systems: Theoretical Developments and Applications, Powder Technology 302 (2016) 108–152. doi:10.1016/j.powtec.2016.07.010.
URL http://dx.doi.org/10.1016/j.powtec.2016.07.010http://linkinghub.elsevier.com/retrieve/pii/S0032591016304065

[13] J. R. Williams, A. P. Pentland, Superquadrics and modal dynamics for discrete elements in interactive design, Engineering Computations 9 (2) (1992) 115–127. doi:10.1108/eb023852.
URL http://www.emeraldinsight.com/doi/abs/10.1108/eb023852http://www.emeraldinsight.com/doi/10.1108/eb023852

[14] T. Matsushima, H. Saomoto, Discrete element modeling for irregularly-shaped sand grains, Proc. NUMGE2002: Numerical methods in geotechnical engineering, Mestat (ed.) (2002) 239–246.

[15] M. M. Shamsi, A. Mirghasemi, Numerical simulation of 3d semi-real-shaped granular particle assembly, Powder technology 221 (2012) 431–446.

[16] H. Ouafdel, Numerical simulations of granular assemblies with three-dimensional ellipsoid-shaped particles, Ph.D. thesis (1998).
URL http://hdl.handle.net/10012/331

[17] H. Kruggel-Emden, S. Rickelt, S. Wirtz, V. Scherer, A study on the validity of the multi-sphere Discrete Element Method, Powder Technology 188 (2) (2008) 153–165. doi:10.1016/j.powtec.2008.04.037.
URL http://linkinghub.elsevier.com/retrieve/pii/S0032591008002143

[18] D. Höhner, S. Wirtz, H. Kruggel-Emden, V. Scherer, Comparison of the multi-sphere and polyhedral approach to simulate non-spherical particles within the discrete element method: Influence on temporal force evolution for multiple contacts, Powder Technology 208 (3) (2011) 643–656. doi:10.1016/j.powtec.2011.01.003.
URL http://linkinghub.elsevier.com/retrieve/pii/S0032591011000209

[19] D. Höhner, S. Wirtz, V. Scherer, A numerical study on the influence of particle shape on hopper discharge within the polyhedral and multi-sphere discrete element method, Powder Technology 226 (2012) 16–28. doi:10.1016/j.powtec.2012.03.041.
URL http://linkinghub.elsevier.com/retrieve/pii/S0032591012002094

[20] D. Höhner, S. Wirtz, V. Scherer, Experimental and numerical investigation on the influence of particle shape and shape approximation on hopper discharge using the discrete element method, Powder Technology 235 (2013) 614–627. doi:10.1016/j.powtec.2012.11.004.
URL http://linkinghub.elsevier.com/retrieve/pii/S003259101200753X

[21] P. W. Cleary, M. L. Sawley, DEM modelling of industrial granular flows: 3D case studies and the effect of particle shape on hopper discharge, Applied Mathematical Modelling 26 (2) (2002) 89–111. doi:10.1016/S0307-904X(01)00050-6.

[22] G. G. Pereira, P. W. Cleary, Segregation due to particle shape of a granular mixture in a slowly rotating tumbler, Granular Matter 19 (2). doi:10.1007/s10035-017-0708-7.

[23] F. Y. Fraige, P. A. Langston, G. Z. Chen, Distinct element modelling of cubic particle packing and flow, Powder Technology 186 (3) (2008) 224–240. doi:10.1016/j.powtec.2007.12.009.

[24] J. Härtl, J. Y. Ooi, Numerical investigation of particle shape and particle friction on limiting bulk friction in direct shear tests and comparison with experiments, Powder Technology 212 (1) (2011) 231–239. doi:10.1016/j.powtec.2011.05.022.
URL http://dx.doi.org/10.1016/j.powtec.2011.05.022

[25] H. Tao, B. Jin, W. Zhong, X. Wang, B. Ren, Y. Zhang, R. Xiao, Discrete element method modeling of non-spherical granular flow in rectangular hopper, Chemical Engineering and Processing: Process Intensification

49 (2) (2010) 151–158. doi:10.1016/j.cep.2010.01.006.
URL http://dx.doi.org/10.1016/j.cep.2010.01.006

[26] DEM Solutions Ltd., EDEM 2.4 Programming Guide (2011) 49.

[27] N. V. Brilliantov, F. Spahn, J.-M. Hertzsch, T. Pöschel, Model for collisions in granular gases, Physical Review E 53 (5) (1996) 5382–5392. doi:10.1103/PhysRevE.53.5382.
URL https://link.aps.org/doi/10.1103/PhysRevE.53.5382

[28] R. Mindlin, H. Deresiewicz, Elastic Spheres in Contact under Varying Oblique Force, Journal of Applied Mechanics 20 (1953) 327–344.

[29] C. Kloss, C. Goniva, A. Hager, S. Amberger, S. Pirker, Models, algorithms and validation for opensource DEM and CFD-DEM, Progress in Computational Fluid Dynamics, An International Journal 12 (2/3) (2012) 140. doi:10.1504/PCFD.2012.047457.
URL http://www.inderscience.com/link.php?id=47457

[30] A. Di Renzo, F. P. Di Maio, Comparison of contact-force models for the simulation of collisions in DEM-based granular flow codes, Chemical Engineering Science 59 (2004) 525–541. doi:10.1016/j.ces.2003.09.037.

[31] L. Benvenuti, Establishing the predictive capabilities of DEM simulations: sliding and rolling friction coefficients of non-spherical particles, in: CFD 2014 Proceedings, no. June, 2014, pp. 1–7.

[32] A. H. Barr, Superquadrics and angle-preserving transformations, IEEE Computer Graphics and Applications 1 (January) (1981) 11–23. doi:10.1109/MCG.1981.1673799.

[33] C. Zhou, J. Y. Ooi, Numerical investigation of progressive development of granular pile with spherical and non-spherical particles, Mechanics of Materials 41 (6) (2009) 707–714. doi:10.1016/j.mechmat.2009.01.017.
URL http://linkinghub.elsevier.com/retrieve/pii/S0167663609000209

[34] I. Goldhirsch, Stress, stress asymmetry and couple stress: from discrete particles to continuous fields, Granular Matter 12 (3) (2010) 239–252.

[35] T. Weinhart, C. Labra, S. Luding, J. Y. Ooi, Influence of coarse-graining parameters on the analysis of DEM simulations of silo flow, Powder Technology 293 (November) (2015) 138–148. doi:10.1016/j.powtec.2015.11.052.
URL http://dx.doi.org/10.1016/j.powtec.2015.11.052

[36] M. Kodam, R. Bharadwaj, J. Curtis, B. Hancock, C. Wassgren, Force model considerations for glued-sphere discrete element method simulations, Chemical Engineering Science 64 (15) (2009) 3466–3475. doi:10.1016/j.ces.2009.04.025.

URL http://www.sciencedirect.com/science/article/pii/S0009250909002747http://linkinghub.elsevier.com/retrieve/pii/S0009250909002747

[37] J. Ai, J.-F. Chen, J. M. Rotter, J. Y. Ooi, Assessment of rolling resistance models in discrete element simulations, Powder Technology 206 (3) (2011) 269–282. doi:10.1016/j.powtec.2010.09.030.
URL http://linkinghub.elsevier.com/retrieve/pii/S0032591010005164

[38] C. M. Wensrich, A. Katterfeld, Rolling friction as a technique for modelling particle shape in DEM, Powder Technology 217 (2012) 409–417. doi:10.1016/j.powtec.2011.10.057.
URL http://dx.doi.org/10.1016/j.powtec.2011.10.057

[39] A. Aigner, S. Schneiderbauer, C. Kloss, S. Pirker, Determining the coefficient of friction by shear tester simulation, in: 3rd International Conference on Particle-Based Methods, Vol. 1, 2013, pp. 335–342.

[40] D. M. Wood, Soil behaviour and critical state soil mechanics, Cambridge university press, 1990.

[41] A. Altunbas, B. Soltanbeigi, O. Cinicioglu, Determination of active failure surface geometry for cohesionless backfills, Geomechanics and Engineering 12 (6) (2017) 965–981.

[42] L. Zhang, C. Thornton, A numerical examination of the direct shear test, Geotechnique 57 (4) (2007) 343–354.

[43] W. Beverloo, H. Leniger, J. Van de Velde, The flow of granular solids through orifices, Chemical engineering science 15 (3-4) (1961) 260–269.

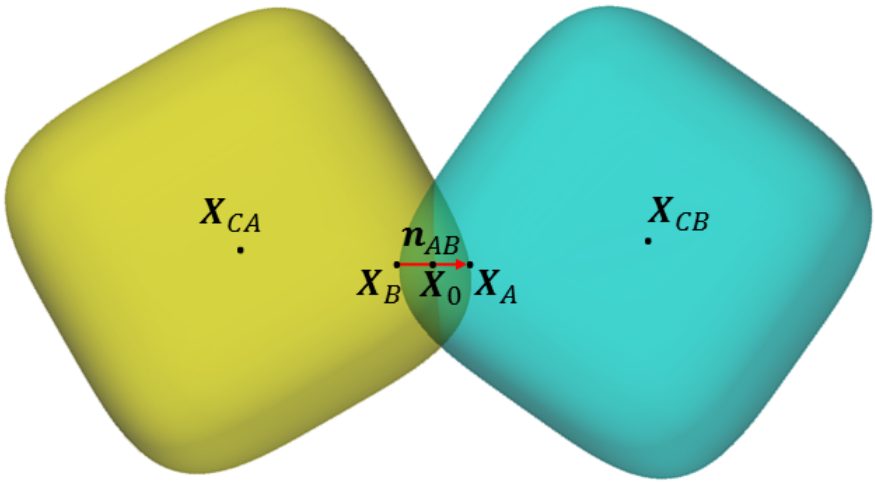

Figure 1: Scheme of particle-particle contact for superquadrics.

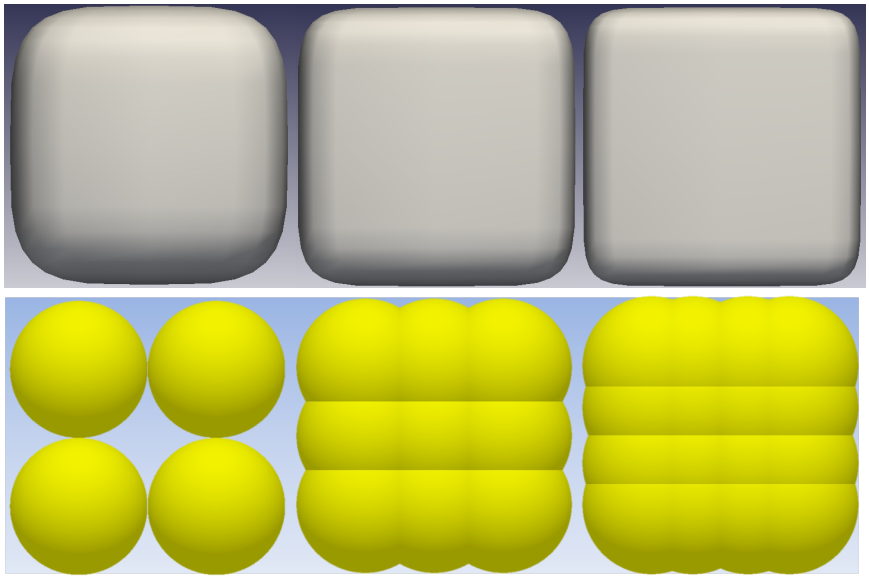

Figure 2: Particle shapes used. SQ($N4$),SQ($N6$) and SQ($N8$), top, from left to right. And MS(8), MS(27) and MS(64), bottom, from left to right.

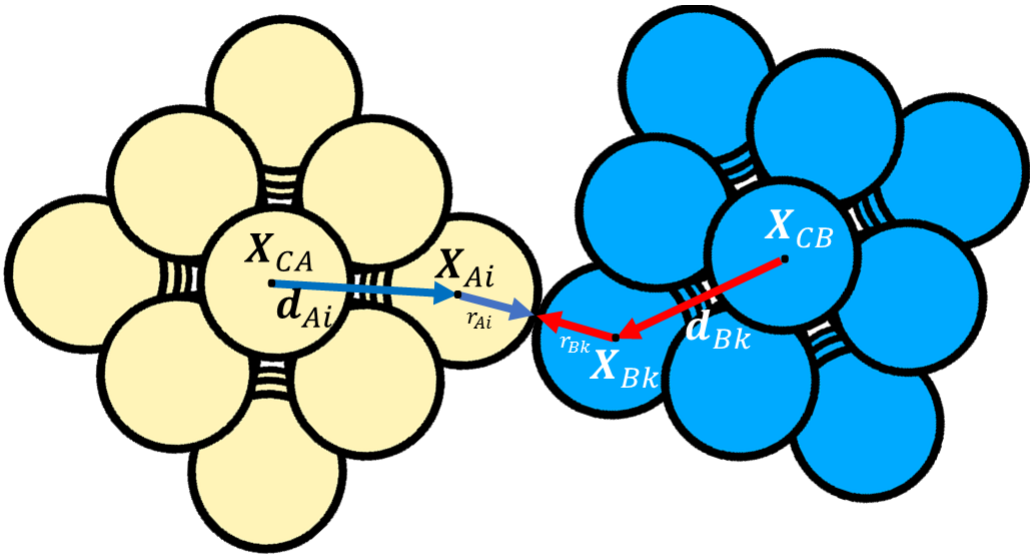

Figure 3: Scheme of particle-particle contact for multi-spheres.

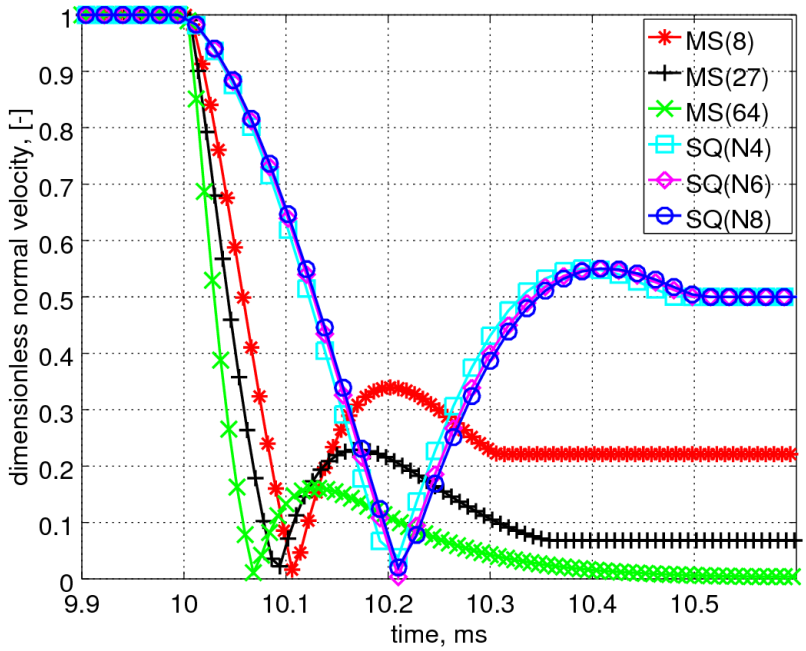

Figure 4: The dimensionless particle velocity v/v_{pre} as a function of time during the particle-wall impact.

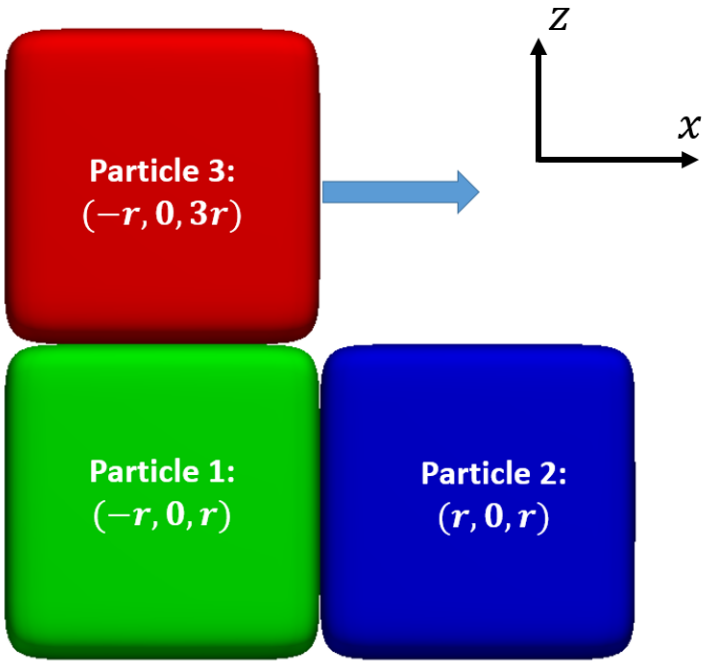

Figure 5: Simulation setup for determining the degree of interlocking.

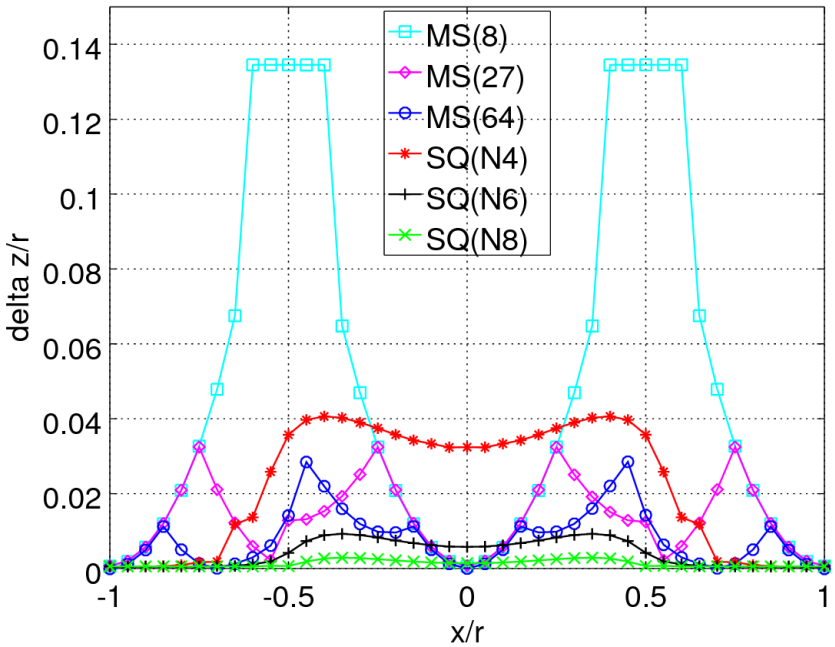

Figure 6: Dimensionless interlocking value $\delta z/r$ as a function of dimensionless x/r-coordinate.

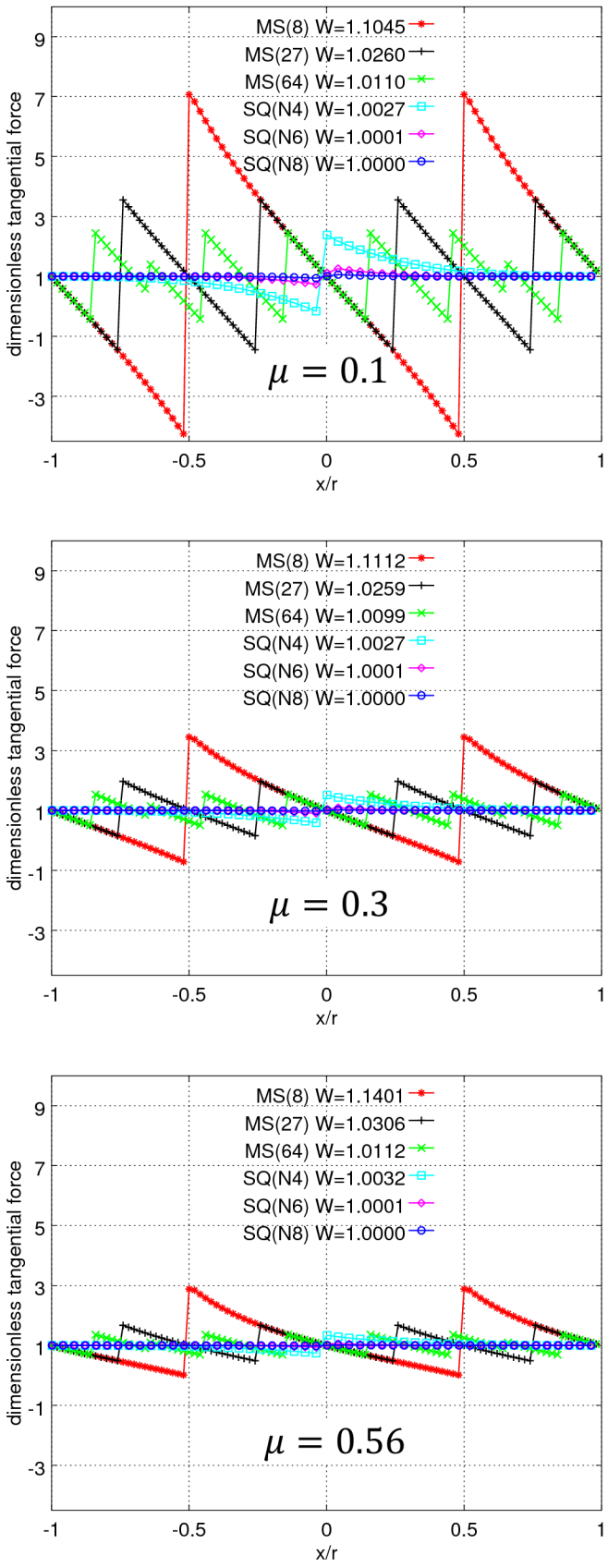

Figure 7: Dimensionless tangential force $F_t/\mu^s_{pp}mg$ as a function of initial dimensionless x/r-coordinate for different coefficients of friction $\mu = 0.1, 0.3, 0.56$.

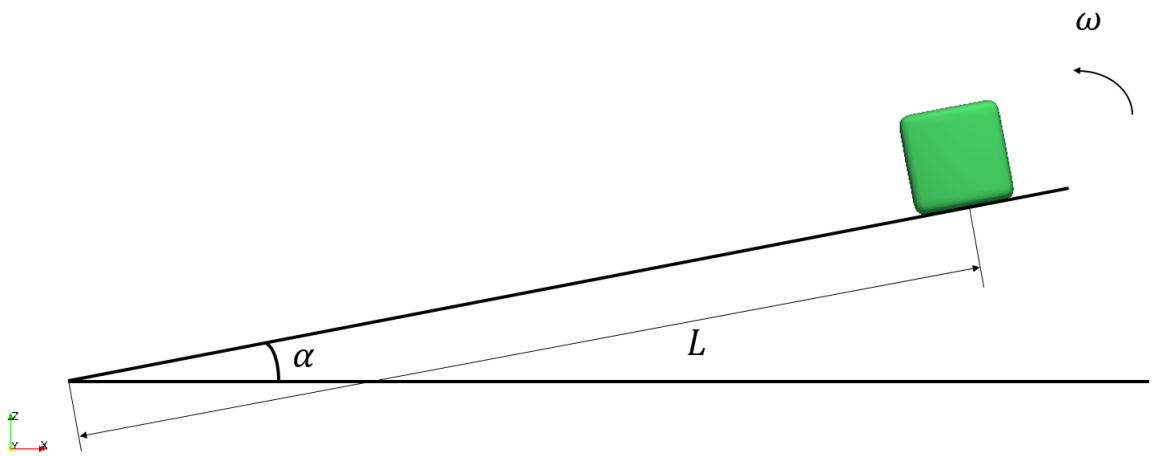

Figure 8: Inclined plate I: setup.

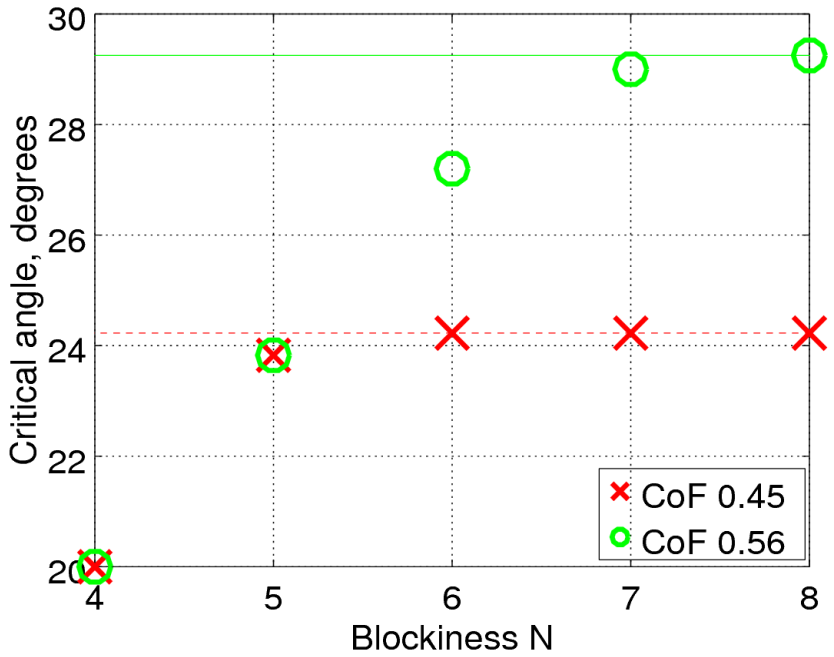

Figure 9: Critical sliding/tilting angle as function of superquadric exponent N (blockiness): cross signs for $\mu_1 = 0.45$ ("CoF 0.45"), green circles for $\mu_2 = 0.56$("CoF 0.56"). The red dash line indicates the sliding angle for $\mu_1 = 0.45$, the green solid line represents the sliding angle for $\mu_2 = 0.56$.

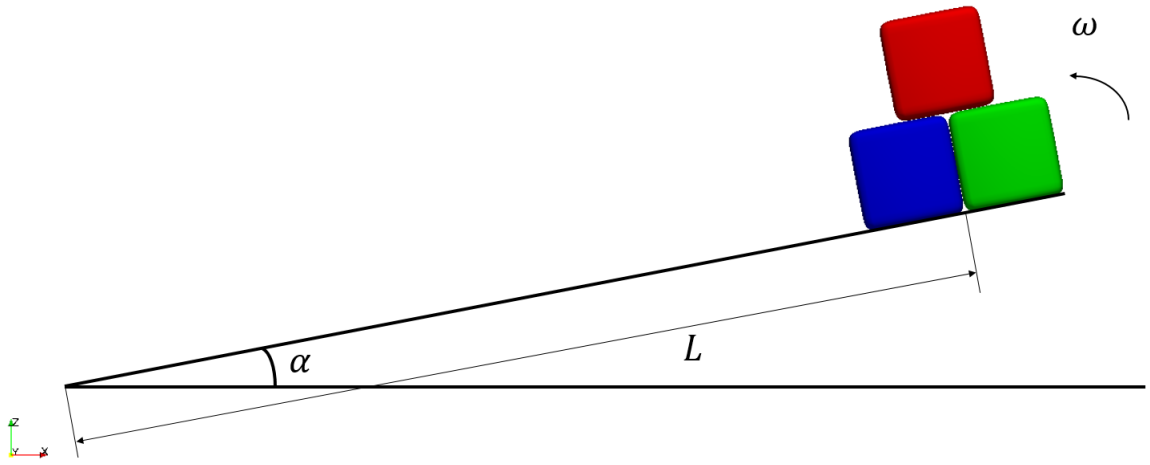

Figure 10: Inclined plate II: particle configuration.

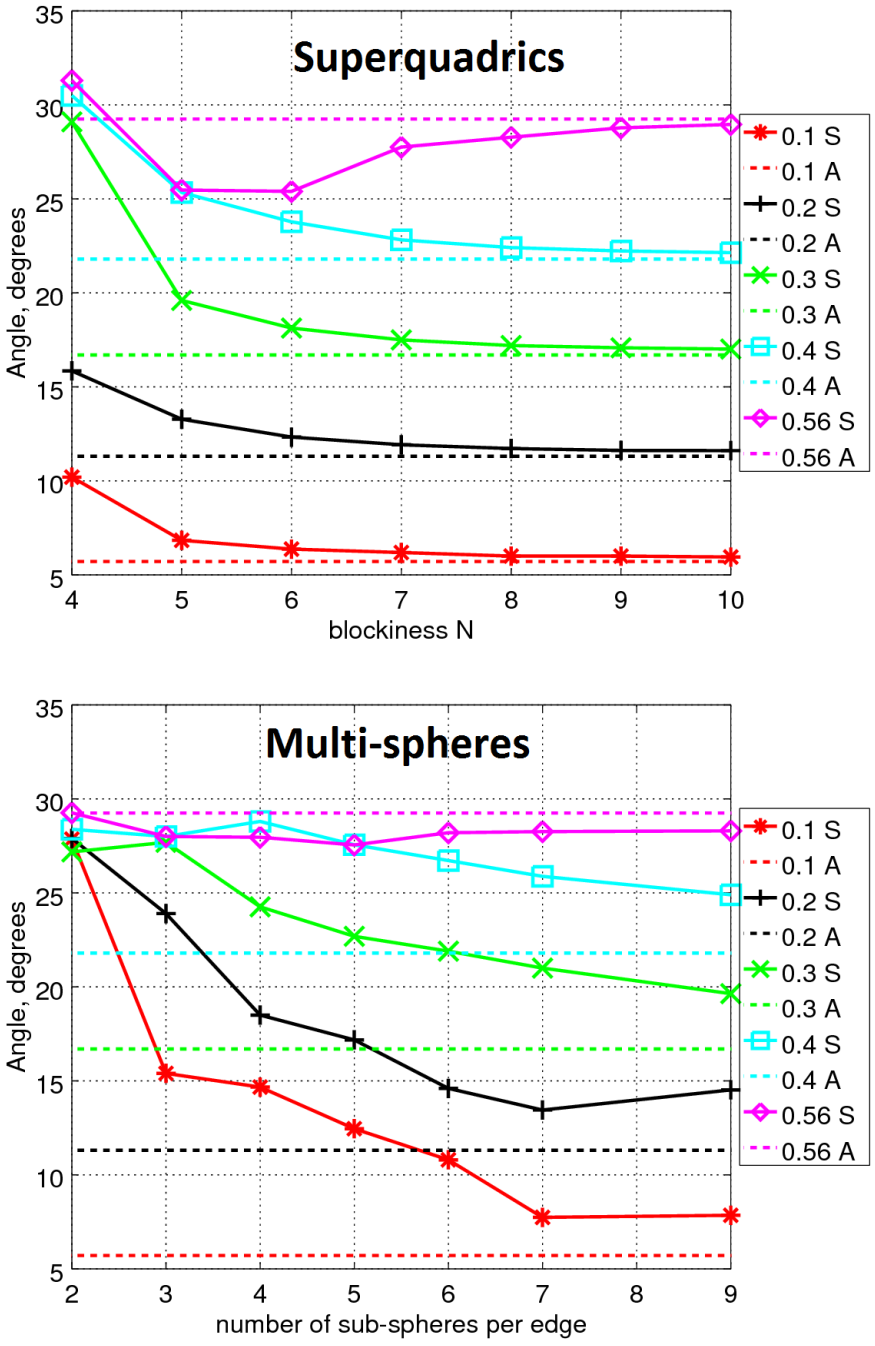

Figure 11: Inclined plate II: simulation results. Critical angle vs. superquadric blockiness vs. number of sub-spheres for MS for different coefficients of friction: $\mu^s_{pp} = 0.1, 0.2, 0.3, 0.4$, and 0.56. "S" stands for simulation, "A" stands for analytical solution in case of ideal cubes (dashed lines).

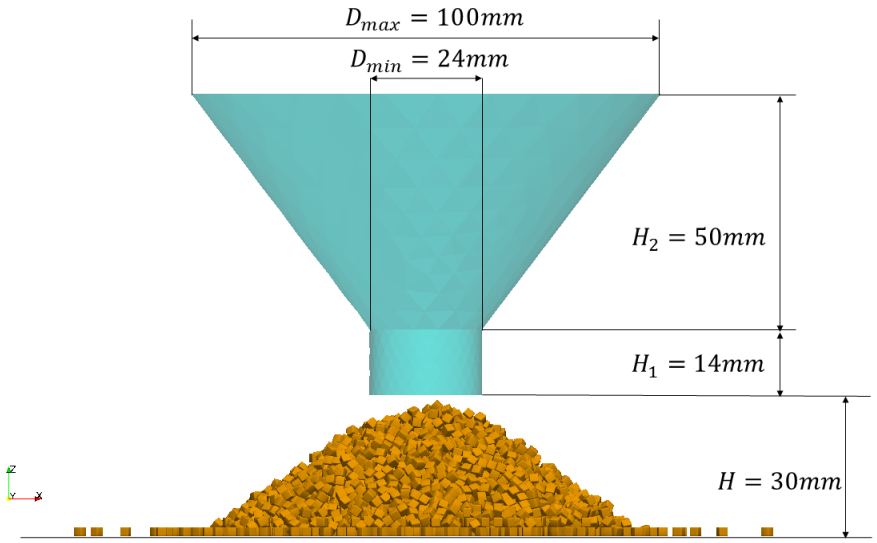

Figure 12: Angle of repose simulation setup.

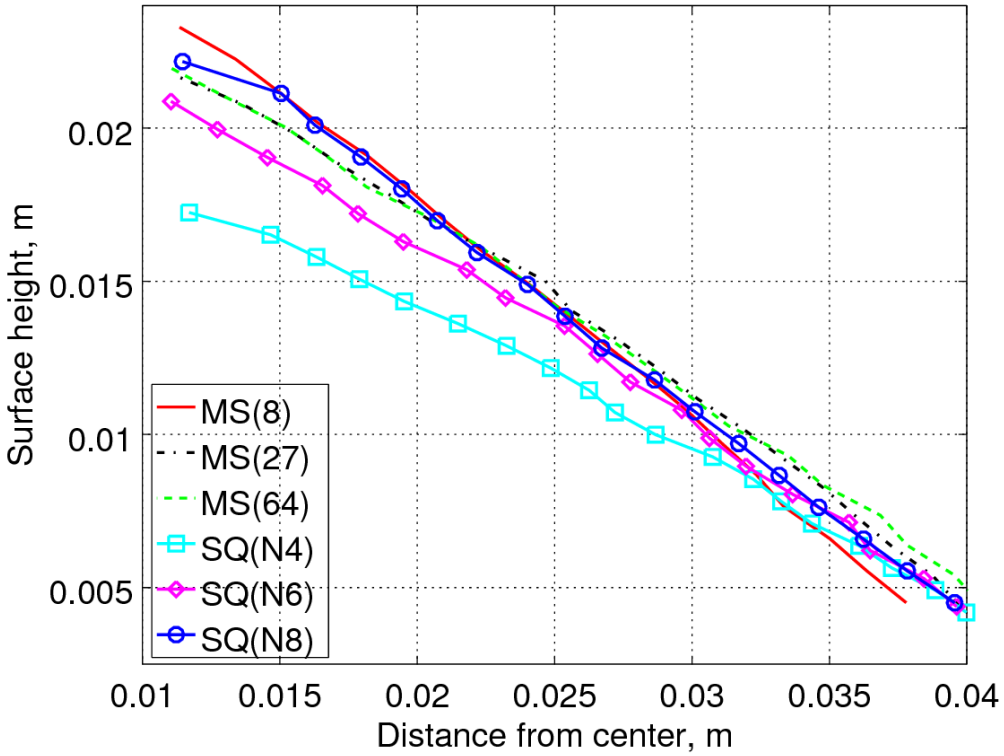

Figure 13: Comparison of the surface profiles of particle piles from MS and SQ simulations.

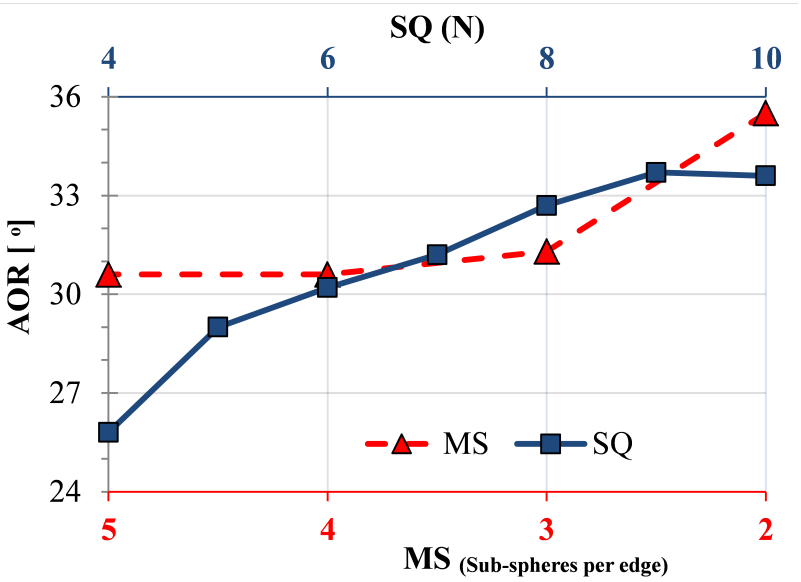

Figure 14: Averaged angle of repose for different MS and SQ particles.

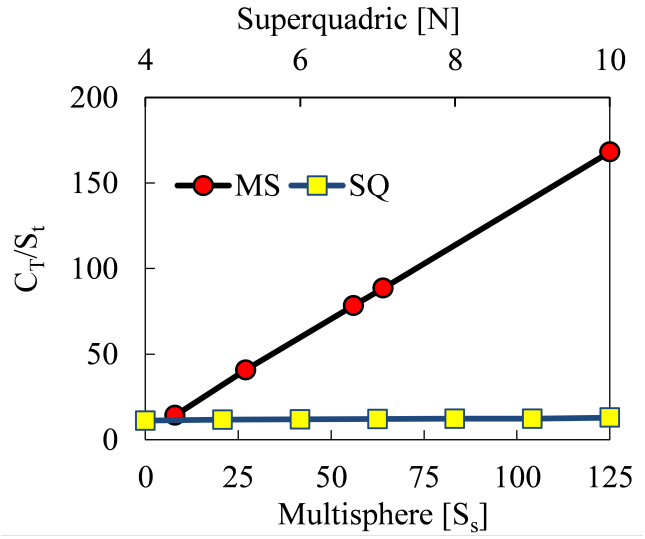

Figure 15: Computational time vs. number of sub-spheres for MS particles and vs. blockiness N for SQ particles.

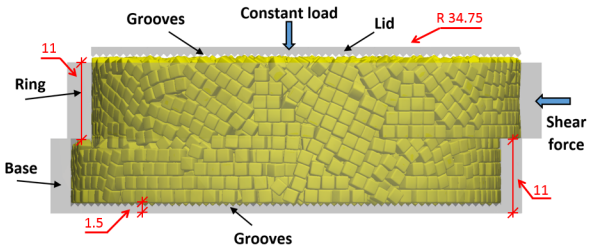

Figure 16: Jenike shear tester filled with superquadric particles (dimensions are in mm).

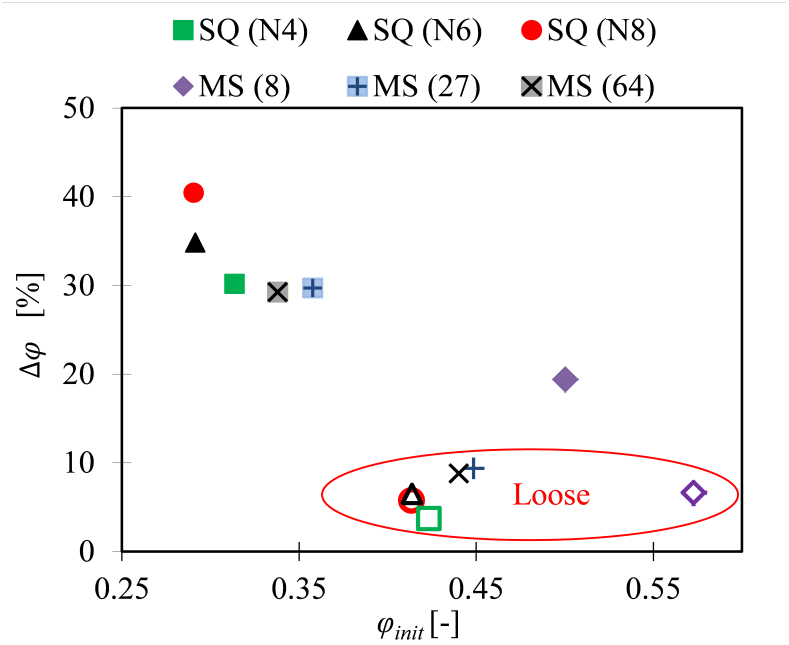

Figure 17: Porosity of the packings with different particle shapes (filled markers are for the dense packing).

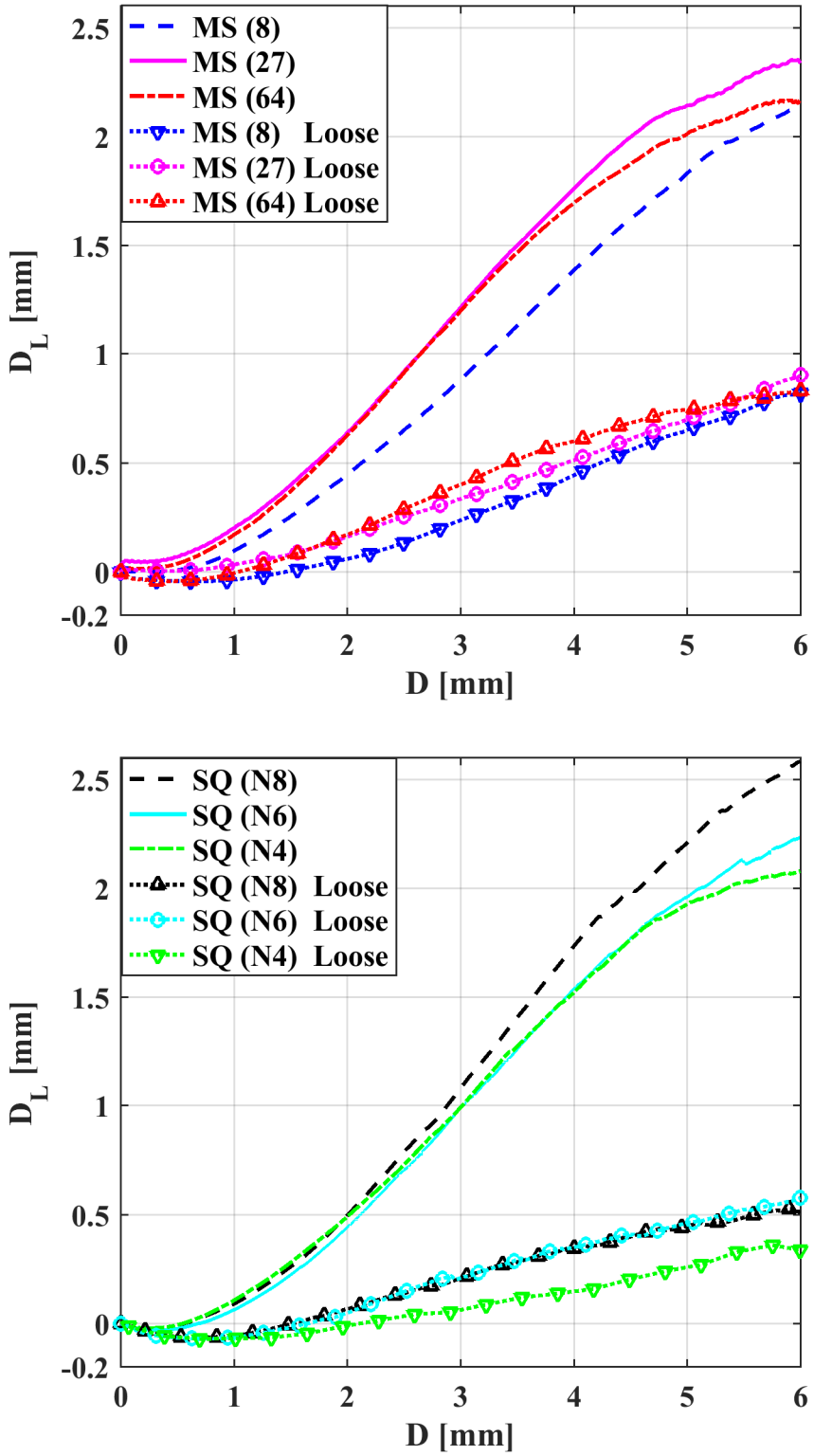

Figure 18: The relative vertical displacement of the lid during the shearing for both loose and dense packing of: a) MS particles; b) SQ particles.

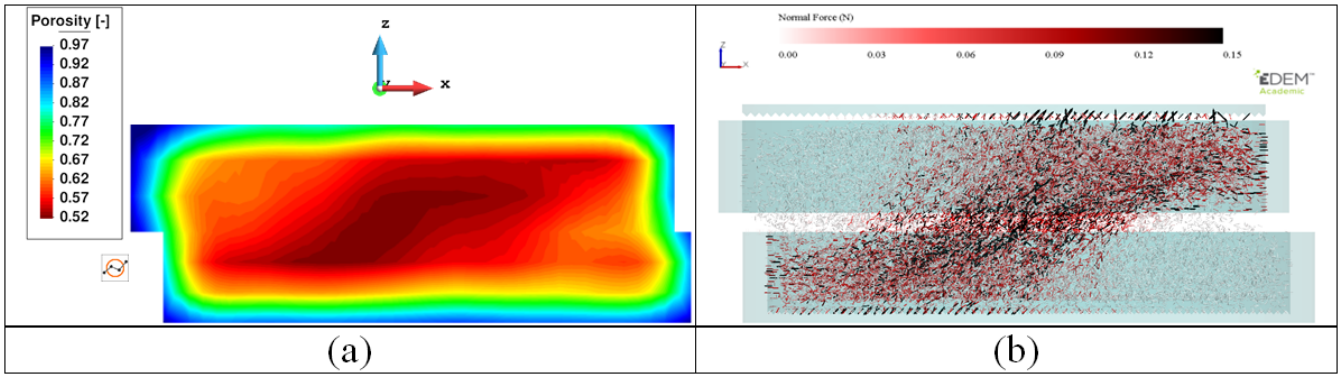

Figure 19: Distribution of the voids and forces inside the Jenike cell a) coarse grained results for visualization of the porosity b) normal contact force network (note that results are for MS8, and for displacement of $D = 6$ mm).

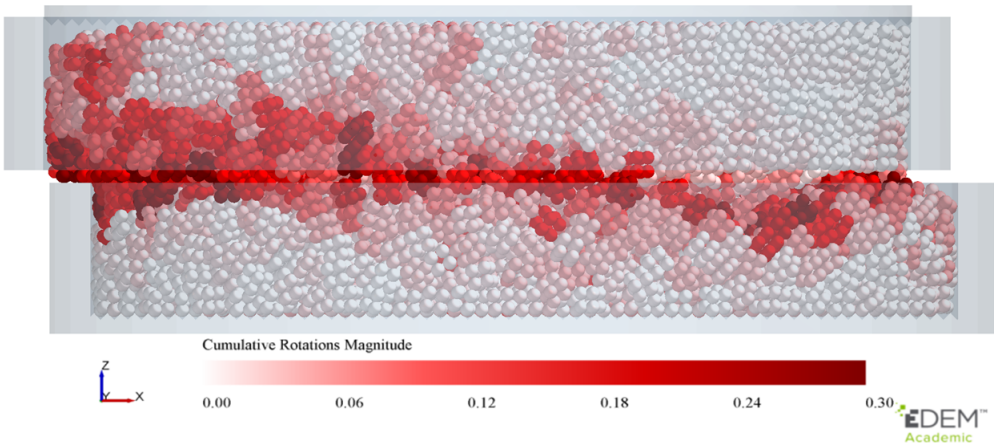

Figure 20: Distribution of the cumulative rotation magnitude for MS(8) particles (at $D = 6$ mm).

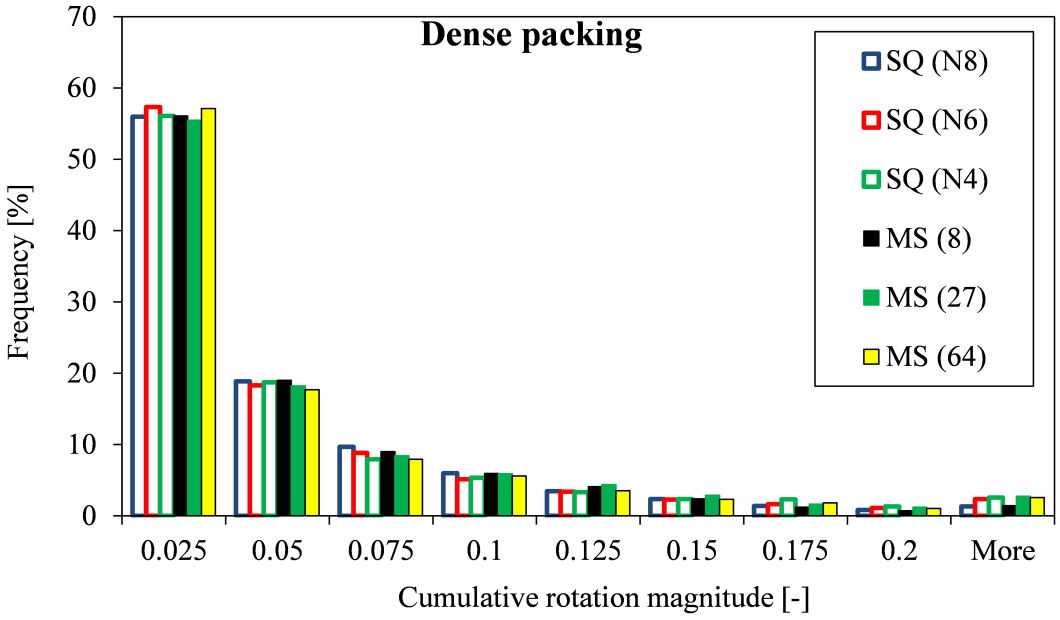

Figure 21: Cumulative rotation magnitude for the dense samples.

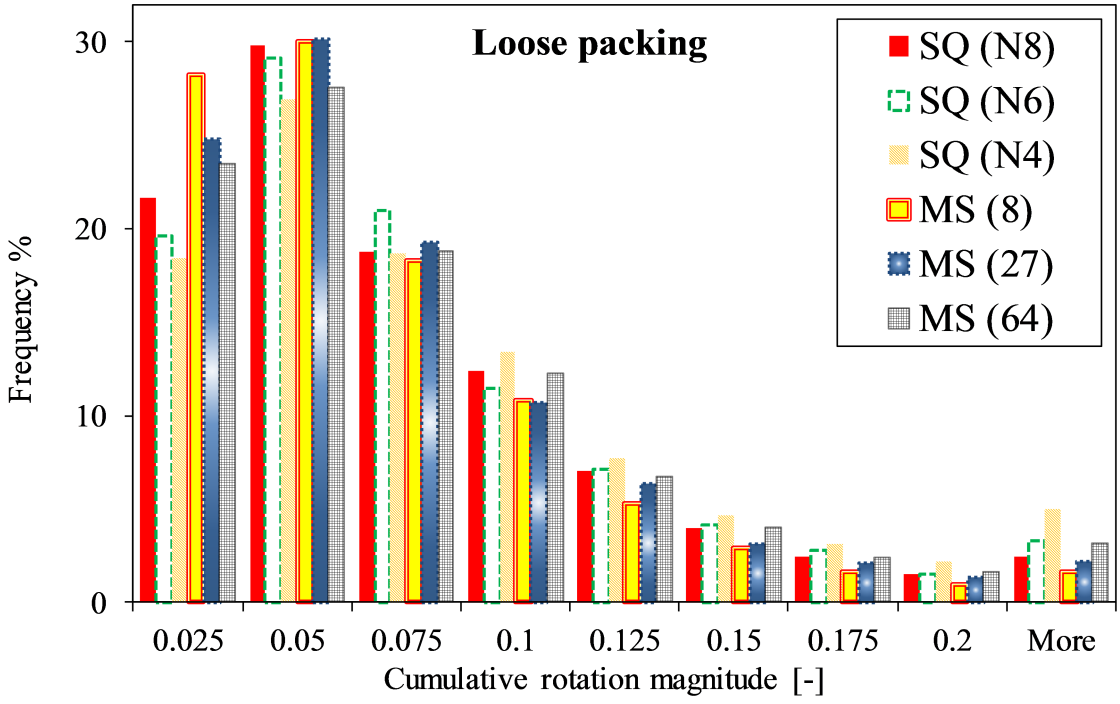

Figure 22: Cumulative rotation for the loose samples.

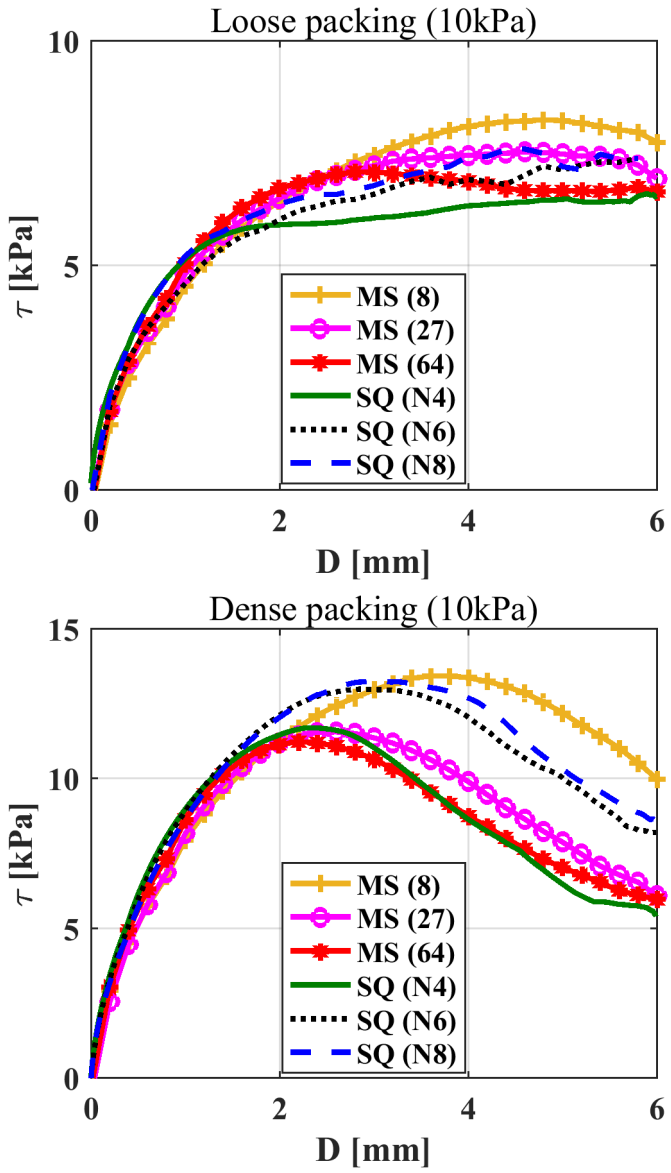

Figure 23: Jenike direct shear simulations considering SQ and MS particles a)loose packings b) dense packings.

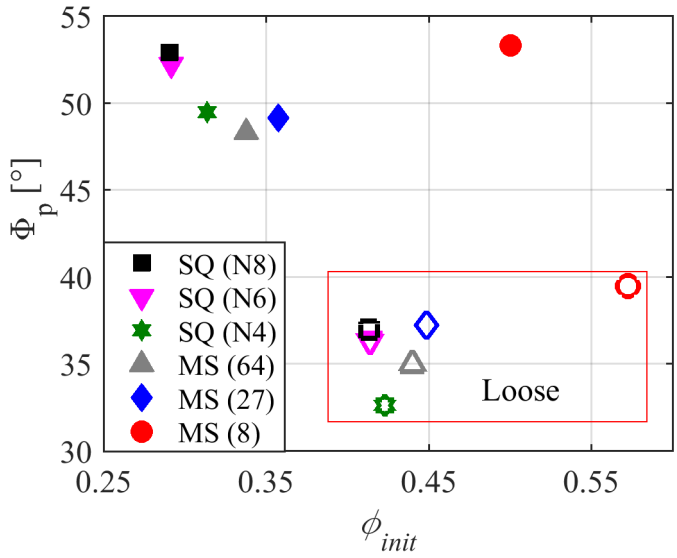

Figure 24: Dependence of the peak friction angle (Φ_p) on both particle shape and the initial porosity of the system (the filled markers are for dense packing).

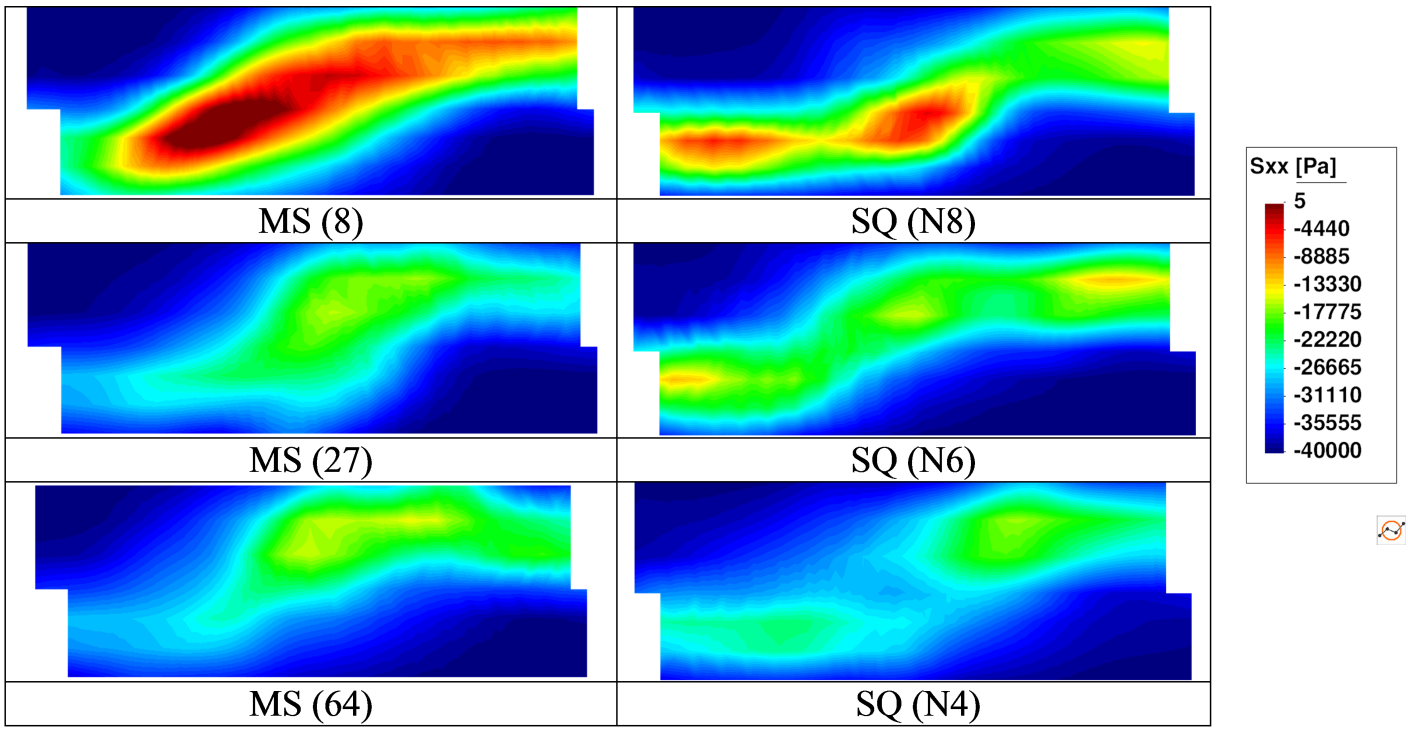

Figure 25: Horizontal stress distribution for MS and SQ particles at $D = 6$ mm.

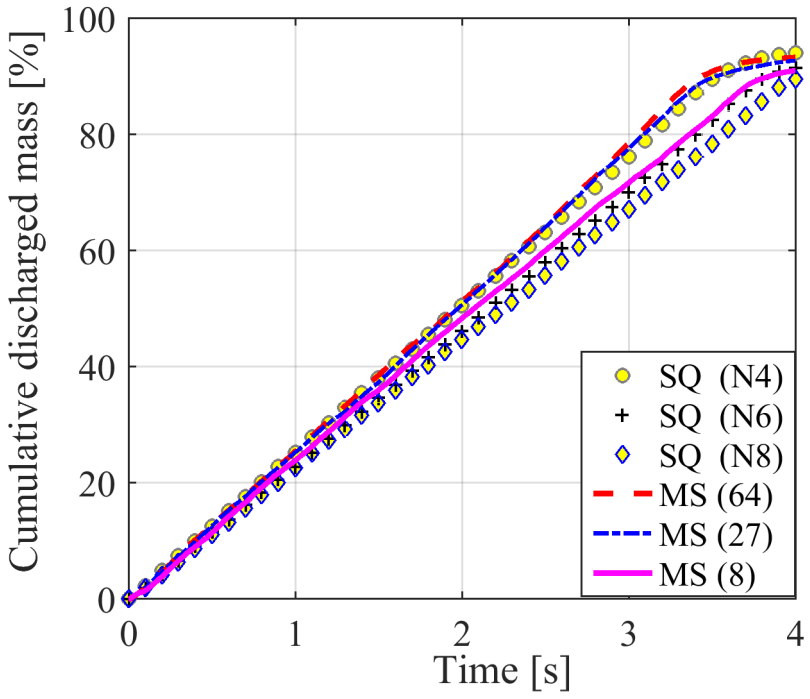

Figure 26: Cumulative discharged mass over time.

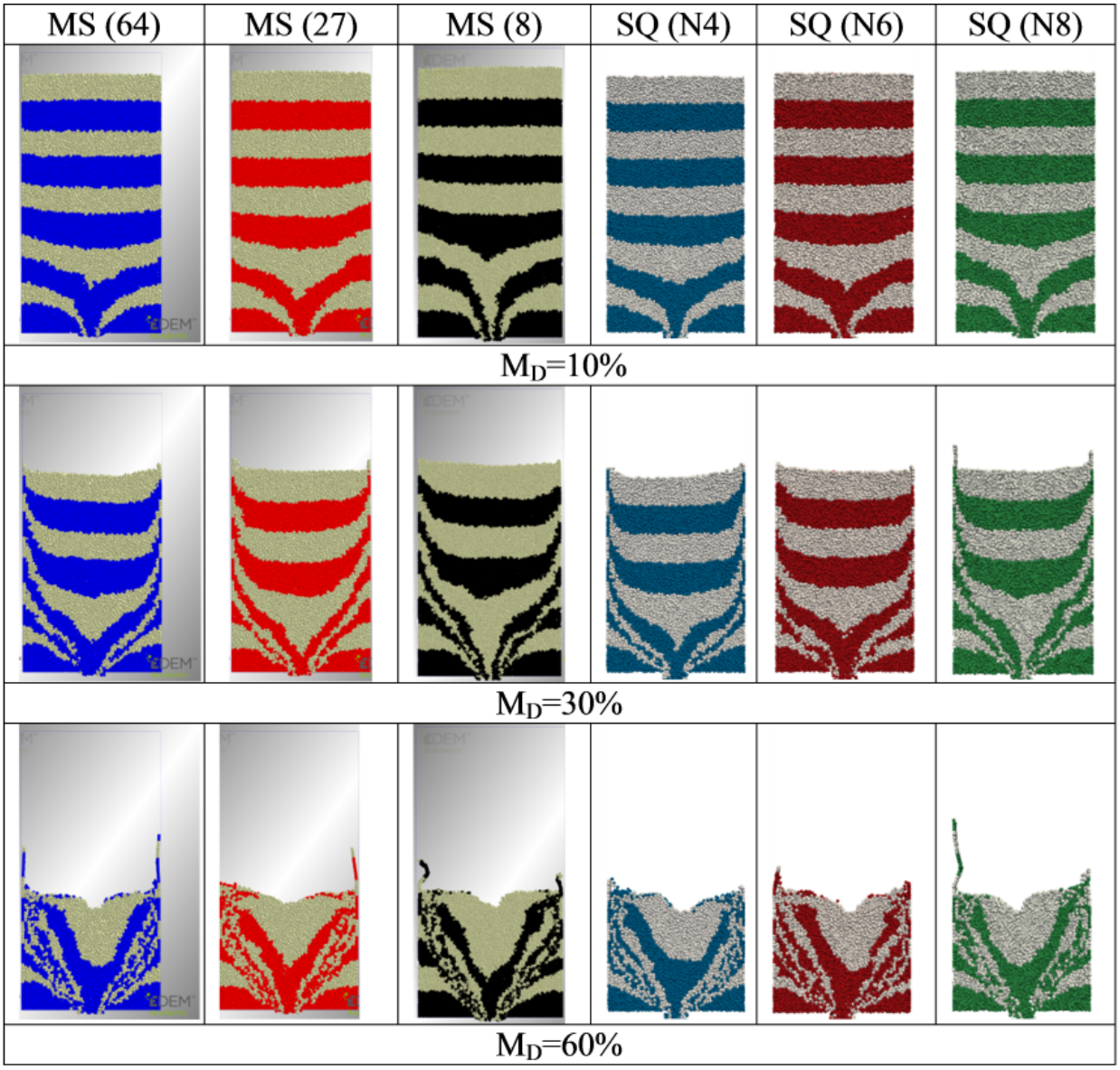

Figure 27: Flow profiles for both SQ and MS particles at M_D =10, 30 and 60 %.

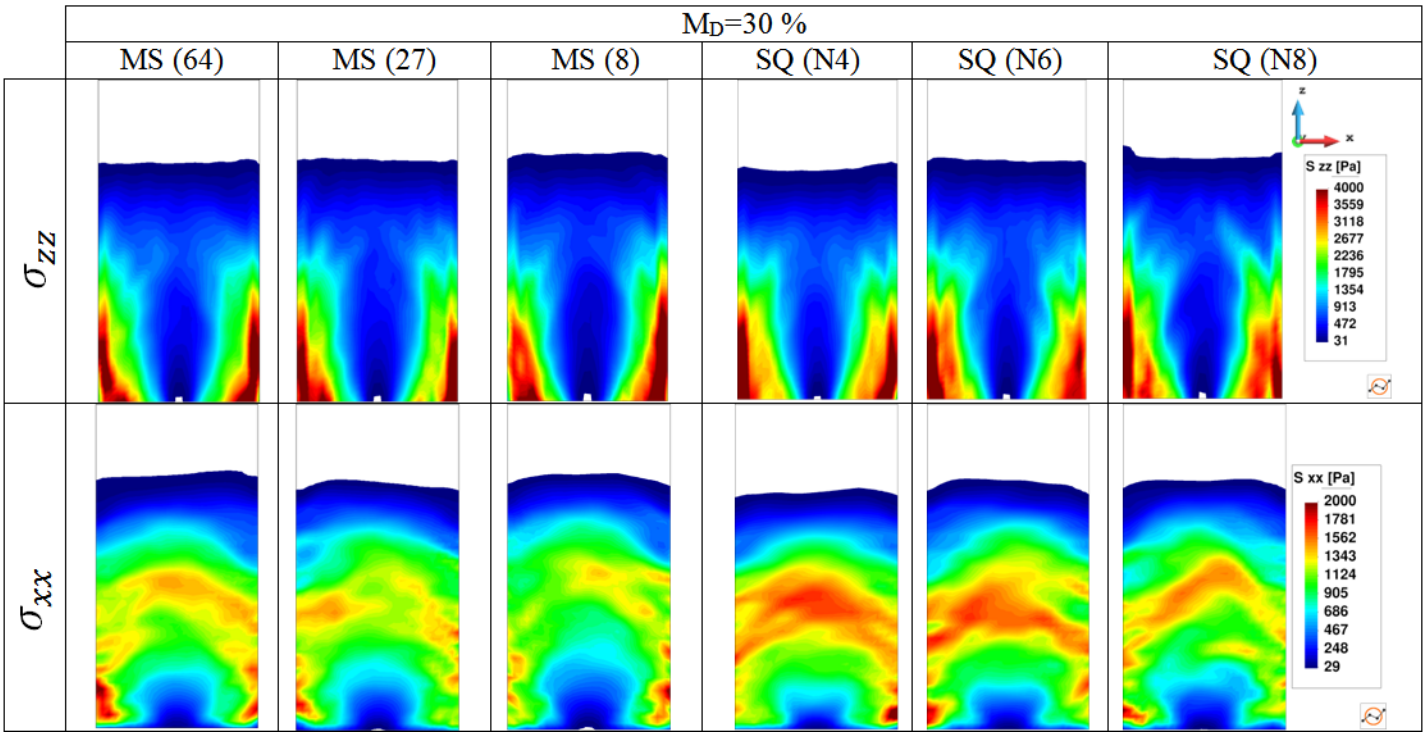

Figure 28: Stress distribution inside the silo at M_D =30 %.

.

Table 1: DEM material properties

Parameter	Value
Density (particle) ρ [kg/m^3]	4100
Coefficient of particle-particle friction μ^s_{pp}	0.56
Coefficient of particle-wall friction μ^s_{pw}	0.45
Coefficient of restitution (particle-particle), ε_p	0.15
Coefficient of restitution (particle-wall), ε_{pw}	0.5
Poisson ratio (particles), ν_p	0.25
Poisson ratio (wall), ν_w	0.25
Shear modulus (particles), G_p[Pa]	10^7
Shear modulus (wall), G_w[Pa]	10^{10}
DEM timestep size, Δt[s]	$2 \cdot 10^{-6}$
Normal force model	Hertz model with viscous damping [27]
Tangential force model	Mindlin-Deresiewicz [28]
Rolling friction model	off

Table 2: Number of particles in Shear test.

Particle	Packing	Number of particles	Total mass, kg
SQ($N4$)	Loose	6163	0.1637
	Dense	7378	0.1960
SQ($N6$)	Loose	5538	0.1637
	Dense	6848	0.2024
SQ($N8$)	Loose	5225	0.1611
	Dense	6576	0.2027
MS(8)	Loose	6236	0.1071
	Dense	7463	0.1282
MS(27)	Loose	5852	0.1540
	Dense	6975	0.1836
MS(64)	Loose	5719	0.1564
	Dense	6920	0.1892

Table 3: Volumes per particle.

Shape	Volume, mm^3	Ratio to volume of ideal cube
SQ($N4$)	6.4819	0.8102
SQ($N6$)	7.2079	0.9010
SQ($N8$)	7.5167	0.9396
MS(8)	4.1933	0.5242
MS(8) (without central void)	4.6649	0.5832
MS(27)	6.4157	0.8020
MS(64)	6.6653	0.8332

Table 4: Number and total mass of particles in silo flow simulation before discharge.

Particle	Number of particles	Total mass, kg
SQ($N4$)	19637	0.5217
SQ($N6$)	17607	0.5205
SQ($N8$)	16652	0.5134
MS(8)	20499	0.5391
MS(27)	18864	0.4965
MS(64)	18475	0.5052